Received: 13 July 2024 | Revised: 27 September 2024 | Accepted: 28 October 2024

DOI: 10.1111/jmi.13369

Journal of Microscopy RMS

ORIGINAL ARTICLE

In situ isotropic 3D imaging of vasculature perfusion specimens using x-ray microscopic dual-energy CT

Stephan Handschuh | **Ursula Reichart** | **Stefan Kummer** | **Martin Glösmann**

VetCore Facility for Research/Imaging Unit, University of Veterinary Medicine Vienna, Vienna, Austria

Correspondence
Stephan Handschuh, VetCore Facility for Research/Imaging Unit, University of Veterinary Medicine Vienna, Veterinärplatz 1, 1210 Vienna, Austria.
Email: stephan.handschuh@vetmeduni.ac.at

Funding information
University of Veterinary Medicine Vienna

Abstract

Ex vivo x-ray angiography provides high-resolution, three-dimensional information on vascular phenotypes down to the level of capillaries. Sample preparation for ex vivo angiography starts with the removal of blood from the vascular system, followed by perfusion with an x-ray dense contrast agent mixed with a carrier such as gelatine or a polymer. Subsequently, the vascular micro-architecture of harvested organs is imaged in the intact fixed organ. In the present study, we present novel microscopic dual-energy CT (microDECT) imaging protocols that allow to visualise and analyse microvasculature in situ with reference to the morphology of hard and soft tissue. We show that the spectral contrast of µAngiofil and Micropaque barium sulphate in perfused specimens allows for the effective separation of vasculature from mineralised skeletal tissues. Furthermore, we demonstrate the counterstaining of perfused specimens using established x-ray dense contrast agents to depict blood vessels together with the morphology of soft tissue. Phosphotungstic acid (PTA) is used as a counterstain that shows excellent spectral contrast in both µAngiofil and Micropaque barium sulphate–perfused specimens. A novel Sorensen-buffered PTA protocol is introduced as a counterstain for µAngiofil specimens, as the polyurethane polymer is susceptible to artefacts when using conventional staining solutions. Finally, we demonstrate that counterstained samples can be automatically processed into three separate image channels (skeletal tissue, vasculature and stained soft tissue), which offers multiple new options for data analysis. The presented microDECT workflows are suited as tools to screen and quantify microvasculature and can be implemented in various correlative imaging pipelines to target regions of interest for downstream light microscopic investigation.

KEYWORDS
µAngiofil, µCT, barium sulphate, microCT, microvessels, perfusion, post-mortem angiography, vascular imaging

1 | INTRODUCTION

Tomographic x-ray imaging of the cardiovascular system (CT angiography) is widely used in clinical settings to facilitate the diagnosis of different vascular disorders[1–3] and involves the use of x-ray dense contrast agents supplied to the bloodstream.[4,5] It is similarly exploited in small laboratory animal models using in vivo microscopic x-ray computed tomography (microCT).[6–8] Laboratory microCT set-ups provide spatial resolution in the micron range; however, animal size, animal motion and radiation dose ultimately limit the resolution of preclinical vascular imaging in vivo. Compared to in vivo imaging approaches, ex vivo angiography—reviewed in Grabherr et al.[9]—can provide much higher spatial image resolution[10] and thus information down to the level of small vessels and capillaries.[11,12] Sample preparation for ex vivo angiography starts with the removal of blood from the vascular system followed by perfusion with a contrast agent mixed with a carrier such as gelatine,[13] silicone[14] or a polymer.[11] Subsequently, the vascular micro-architecture of body regions or harvested organs can be imaged at high contrast due to the high x-ray density of the contrast agent. Different contrast agents have been used for ex vivo angiography, including barium (custom barium sulphate mixtures: Refs. [15, 16]; commercial barium sulphate mixture Micropaque: Refs. [13, 17, 18]), iodine (Angiofil: Refs. [19, 20]; commercial μAngiofil: Refs. [11, 12, 21, 22]), lead (custom lead oxide mixture: Refs. [23]; commercial lead chromate/lead sulphate mixture Microfil: Refs. [24–27]) and bismuth (commercial Vascupaint: Ref. [14]). Alternatively, polymers have been used to create corrosion casts for imaging vascular architecture by scanning electron microscopy (SEM)[28] or microCT.[29]

Laboratory microCT imaging generates 3D image volumes from biological objects ranging in size from 1 mm (or even less) to several centimetres and does not rely on optical transparency. In the laboratory setting, a microfocus x-ray source emitting a polychromatic photon energy spectrum is used for imaging. This spectrum is dependent on (1) the x-ray source target material, (2) the applied tube voltage (kVp) and (3) optionally, an x-ray filter which is placed between the x-ray source and object.[30] Traditionally, microCT imaging is restricted to the acquisition of a single-image volume representing the attenuation of x-rays inside a sample consisting of different materials and at a given polychromatic energy spectrum. Thus, chemical information on material composition is not directly available in conventional radiography and tomography.[31] However, different approaches allow the separation of chemical elements based on their different spectral x-ray attenuation properties, including scanning the same specimen with two x-ray spectra (known as dual-energy CT [DECT]),[32, 33] and recording spectral profiles for each detector pixel by using a multispectral or hyperspectral x-ray detector.[34] Hyperspectral x-ray imaging, albeit capable of discriminating multiple chemical elements within biological samples,[35] is still limited in spatial resolution. In comparison, DECT typically allows to separate only two to three chemical elements and requires knowledge of the chemical composition of the sample to choose a suitable energy pair for imaging. DECT has been exploited both in clinical[36–38] and preclinical[24, 39–41] settings. More recently, microscopic dual-energy CT (microDECT) protocols were established and validated for imaging of fixed tissue biopsies down to spatial resolutions of less than 10 μm with conventional laboratory microCT set-ups.[42]

Utilising microDECT also for the imaging of vascular perfusion specimens may be helpful for two reasons. First, it could be used for spectrally separating perfused blood vessels from mineralised tissue. This is frequently used in clinical DECT and known as 'bone removal'[43,44] and has been recently introduced also for postmortem microCT angiography and virtual autopsy of foetuses and stillborn infants.[45] It was also demonstrated ex vivo on a Microfil-perfused rat using a cone beam CT scanner[24]; however, the high scan energies used in this study (96 kVp/140 kVp) necessary for separating bone from the lead-based contrast agent are not suitable for imaging smaller samples such as mouse organs. Bone removal requires a contrast agent with spectral x-ray absorption properties different from the mineral in bone and teeth (hydroxyapatite [HA]). Second, microDECT imaging of vascular perfusion specimens could be used for separating blood vessels from soft tissue, with the benefit of enabling the interpretation of microvasculature in its tissue context. Generally, non-mineralised biological tissues show low x-ray contrast when imaged in aqueous environments such as PBS, whereas contrast is increased by drying,[46] dehydration[47] or staining with x-ray dense contrast agents[48] (for a more detailed discussion on soft tissue contrast enhancement strategies, see Ref. [49]). Especially, the latter has been proven useful for biological samples, and different compounds have been utilised successfully for soft tissue contrast enhancement, including compounds containing bromine,[50] gadolinium,[51,52] gold,[53] iodine,[48,54] lead,[55,56] molybdenum,[57,58] osmium,[59] ruthenium,[60] silver[53] and tungsten.[48,54] Analogous to histological stains, different x-ray dense contrast agents show different binding properties to biomolecules and tissues and thus may be used for different purposes. For example, iodine potassium iodide (Lugol's iodine), elemental iodine, phosphotungstic acid (PTA) or phosphomolybdic acid show unspecific binding to different tissues and thus are utilised as overview stains.[48,54,61,62] Others exhibit more specific binding such as lead acetate for cell nuclei[55,56] or ruthenium red for proteoglycans in cartilage matrix.[60]

Like in 'bone removal', dual-energy imaging of counterstained vascular perfusion specimens requires a contrast agent in the perfusion casting material with spectral x-ray absorption properties different from the soft tissue counterstain.

The aim of this study was to develop protocols for sample preparation and microDECT imaging enabling the spectral separation of perfused vasculature from mineralised or counter-stained soft tissue. Among the currently available casting agents, we identified iodine-containing μAngiofil and barium sulphate–containing Micropaque, due to their x-ray attenuation properties, as most suitable for dual-energy imaging with a commercial lab-based microCT set-up. With both contrast agents, microDECT allows for an effective spectral separation of vasculature from hard or soft tissues. The presented workflows are suited to screen and quantify microvasculature with reference to soft and hard tissue morphology.

2 | METHODS

This section summarises the key aspects on sample preparation, microDECT imaging and image data processing. Technical details are provided in Tables S1–S5. Each specimen shown in the paper and supplements has a unique sample ID (Table), which is referenced both in the text and figure plates; thus, every figure can be easily linked to all relevant aspects of sample preparation (Table S2), image acquisition (Table S3) and image data processing (Tables S4 and S5). Each sample ID consists of the animal number, tissue number and the number of the processing step. We tested imaging protocols for two different perfusion media, which are μAngiofil and Micropaque barium sulphate. The text of this section focuses on μAngiofil-perfused mice (which are shown in Section 3), whereas methods for Micropaque barium sulphate mice are summarised in File S1.

2.1 | Animals

All perfusion and tissue preparation procedures were performed post-mortem and were therefore not subject to permission by license according to Austrian national legislation and EU directive 2010/63/EU. Two adult male C57BL/6N mice were perfused with a casting agent. One mouse was perfused with Micropaque barium sulphate (mouse ID#1) and one mouse with μAngiofil (mouse ID#2). Inhalation euthanasia was performed by an overdose of isoflurane in accordance with international standards and recommendations for humane euthanasia of laboratory animals.[63,64] Details of inhalation euthanasia have been described in a previous study.[35]

2.2 | Perfusion

Ten minutes post-mortem, the thorax was opened, and the left ventricle was cut open with fine scissors. A stainless-steel feeding needle (20-ga, 38 mm, Hugo Sachs Elektronik) was inserted into the left ventricle for antegrade perfusion in the aortic arch and fixed with a tying cord. Subsequently, the right atrium was cut open to enable outflow of blood and perfusion agents. Animals were perfused with 50 mL isotonic saline containing 10 UI/mL heparin (warmed to 35°C), followed by 50 mL neutral buffered formalin (NBF, room temperature [RT], Table S2). Subsequent perfusion with μAngiofil (Fumedica AG) was carried out according to the manufacturer's guidelines. After perfusion, specimens were left for 15 min at RT to allow polymerisation of the polyurethane polymer. Subsequently, the whole mouse was immersed for 72 h in 500 mL NBF at 4°C, transferred to 500 mL PBS/0.1% NaN_3 and stored at 4°C. Select tissues (head, paw, tail) were dissected for imaging. Perfusion with Micropaque barium sulphate is detailed in File S1.

2.3 | MicroDECT imaging

MicroDECT data were acquired with an Xradia MicroXCT-400 (Carl Zeiss X-Ray Microscopy). Image acquisition is detailed in Table S3. The energy pairs for dual-energy imaging were selected so that the *k*-edges of iodine (μAngiofil) and barium (Micropaque) could be utilised (Figure 1, Figure S7). For all μAngiofil-perfused samples, the energy pair used for imaging (40 kVp, 200 μA/80 kVp, 100 μA) showed mean photon energies of the low-energy scan (26.81 keV) and the high-energy scan (41.94 keV) that were below and above the *k*-edge of iodine (33.17 keV), respectively (Figure 1). X-ray attenuation curves and *k*-edges of barium, iodine, calcium and tungsten were adopted from Ref. [65]. X-ray spectra and mean photon energies were simulated for the respective tube voltages (tungsten anode, 0.8 mm glass PYREX filter) using the Siemens online tool for the simulation of x-ray spectra (https://bps.healthcare.siemens-healthineers.com/booneweb/index.html, access date 16.01.2024), which is based on data presented in Refs. [66–68].

2.4 | MicroDECT imaging of μAngiofil-perfused samples to separate vasculature from mineralised tissue

A μAngiofil perfused mouse head (*sample ID 2-1-1*) was mounted in PBS in a plastic container. Details of the source voltages and currents used, detector assembly, x-ray filters, exposure time, angular increment and isotropic voxel

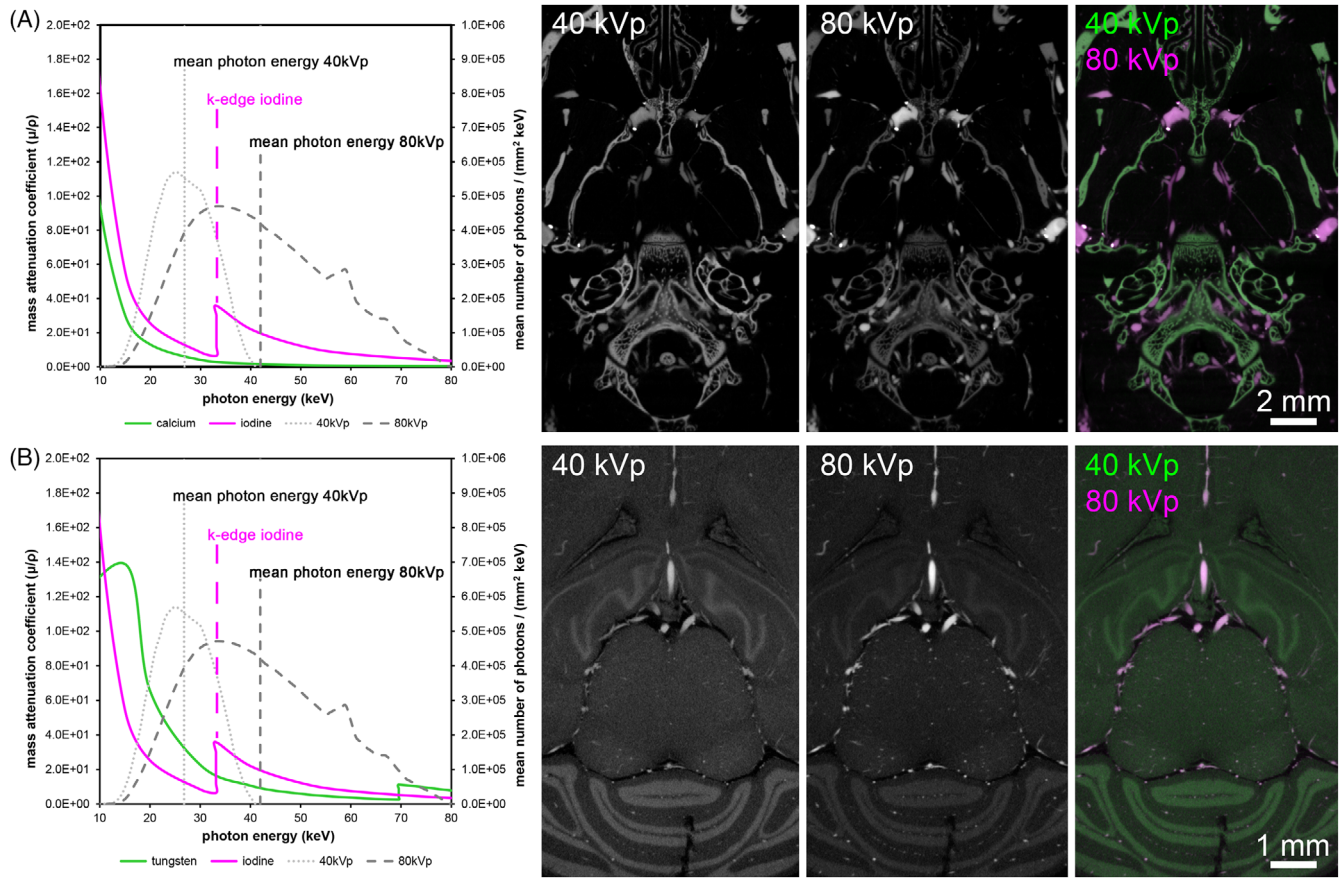

FIGURE 1 X-ray physics background for microscopic dual-energy CT (microDECT) imaging of specimens perfused with iodine containing μAngiofil. (A) MicroDECT imaging of iodine (μAngiofil) versus calcium (hydroxyapatite [HA]) in the mouse head (*sample ID 2-1-1*). The *k*-edge of iodine is at 33.17 keV. The energy pair for imaging (40 kVp/80 kVp) was chosen so that the mean photon energy of the low-energy scan (26.8 keV) was below the *k*-edge of iodine, whereas the mean photon energy of the high-energy scan (41.9 keV) was above the *k*-edge of iodine. The 40 kVp/80 kVp overlay image demonstrates the spectral contrast between μAngiofil-perfused vessels (magenta) and the HA mineral in bone tissue (green). (B) MicroDECT imaging of iodine (μAngiofil) versus tungsten (Sorensen-buffered phosphotungstic acid [B-PTA]) in the mouse brain (*sample ID 2-1-4*). The same energy pair (40 kVp/80 kVp) was chosen for imaging as in (A). The 40 kVp/80 kVp overlay image demonstrates the spectral contrast between μAngiofil-perfused vessels (magenta) and the PTA-stained brain tissue (green).

resolution are listed in Table S3. Three different fields of view (FOVs) were acquired from the sample, including the whole head (FOV1, 0.4X detector assembly), the posterior part of the head and brain (FOV2, 0.4X detector assembly) and part of the nasal cavity (FOV3, 4X detector assembly). In addition, microDECT scans of a paw (*sample ID 2-2-1*) and a piece of tail (*sample ID 2-3-1*) were acquired using the 4X detector assembly. Image volumes were reconstructed with the XMReconstructor software supplied with the scanner and exported in *.TXM format.

2.5 | Counterstaining of soft tissue in μAngiofil-perfused specimens using Sorensen-buffered PTA (B-PTA)

Details on counterstaining are given in Table S2. We used PTA[54,48] to contrast soft tissue. PTA has a much higher *k*-edge than iodine and so cannot contribute to spectral contrast when imaged using a 40 kVp/80 kVp energy pair. We modified original PTA staining protocols that are based on either aqueous or ethanol-based PTA solutions, as detailed below. The rationale is discussed in Section 4.

The μAngiofil-perfused mouse head scanned before (*sample ID 2-1-1*) was skinned, transferred to Sorensen buffer (pH 7.38, Sanova Pharma GesmbH; catalogue number 14562) and immersed in a 2.5% (w/v) solution of PTA hydrate (Merck; Sigma Aldrich catalogue number 455970) in Sorensen buffer. With reference to Sorensen-buffered Lugol's solution known as B-Lugol,[69] the Sorensen-buffered PTA solution will in the following be abbreviated as B-PTA. The mouse head was stained for 4 weeks (28 days) at RT under constant orbital shaking in a volume of 50 mL staining solution. During the staining procedure, the B-PTA solution was replaced twice by a fresh solution.

After staining, the B-PTA-stained mouse head (*sample ID 2-1-2*) was washed in Sorensen buffer to remove unbound contrast agent from tissue. After acquiring microDECT scans from this specimen, the lower jaw, tongue, masseter muscles, salivary glands and eyes were removed to improve image quality when imaging the brain inside the skull (*sample ID 2-1-3*) and another set of microDECT datasets was acquired. Finally, the brain was harvested from the skull (*sample ID 2-1-4*), and another microDECT scan was acquired.

In addition to the mouse head, the mouse paw (*sample ID 2-2-2*) and piece of mouse tail (*sample ID 2-3-2*) were also stained with a 2.5% (w/v) B-PTA solution. Staining times were 9 days for the mouse paw and 10 days for the mouse tail. Both samples were stained in 15 mL B-PTA solution under constant orbital shaking at RT.

2.6 | MicroDECT imaging of µAngiofil-perfused samples to separate vasculature from B-PTA-stained soft tissue

The µAngiofil-perfused and B-PTA-stained mouse brain specimen (*sample ID 2-1-4*) was mounted in a plastic container in Sorensen buffer and imaged with the 0.4X detector assembly. The *k*-edge of tungsten (69.52 keV) did not contribute to spectral contrast with the given energy pair. Details on used source voltage and current, detector assembly, x-ray filter, exposure time, angular increment and isotropic voxel resolution are provided in Table S3. Image volumes were reconstructed with the XMReconstructor software supplied with the scanner and exported in *.TXM format.

2.7 | MicroDECT of µAngiofil-perfused samples for the purpose of separating vasculature from mineralised tissue and B-PTA-stained soft tissue

The µAngiofil-perfused and B-PTA-stained mouse head (*sample ID 2-1-2* and *2-1-3*), mouse paw (*sample ID 2-2-2*) and mouse tail (*sample ID 2-3-2*) specimens were mounted in plastic containers in Sorensen buffer. The *k*-edges of calcium (4.04 keV) and tungsten (69.52 keV) did not contribute to spectral contrast with the given energy pair. Details on used source voltage and current, detector assembly, x-ray filter, exposure time, angular increment and isotropic voxel resolution are provided in Table S3. Image volumes were reconstructed with the XMReconstructor software supplied with the scanner and exported in *.TXM format.

2.8 | MicroDECT image processing and basis material decomposition

The workflow for data processing and basis material decomposition basically follows the workflow described in Handschuh et al.[42] The workflow uses a basis material decomposition algorithm to extract three material fractions from two scan energies, as initially described by Badea et al.[40]

2.8.1 | Image processing and registration

Reconstructed image volumes (*.TXM files) were imported into the 3D software package Amira (FEI Visualization Sciences Group, part of Thermo Fisher Scientific, Mérignac Cédex, FR, versions 2019–2022). First, image intensities were standardised using the *Arithmetic* tool. For conversion, we used the standard Hounsfield unit (HU) formula; however, instead of using water and air as a reference (as described in Handschuh et al.[42]), we here used the respective scanning medium (PBS, agarose or Sorensen buffer) and air as reference. Thus, the standardised image data are strictly not in a HU but in a pseudo-HU (i.e. pseudo-CT numbers) scale. An unsigned 16-bit format was chosen, because the intensity range between −1000 (air) and 0 (scanning medium) did not include information relevant to the aims of the present study. Next, image noise was reduced by image filtering (details of image filters are provided in Table S4). Subsequently, the lower energy scan was anatomically oriented using the *Transform editor*, and the higher energy scan was co-registered (rigid transformation) to the low-energy scan based on normalised mutual information using the tool *Register Images*. This registration step was unavoidable because although the sample was in exactly the same position in the scanner between the two scans, there may be slight shifts in the range of a few pixels due to sample drift. Finally, both scans were resampled using the tool *Resample Transformed Image* (Lanczos interpolation). After registration and resampling, there was a voxel-to-voxel correspondence between the low- and high-energy scans, which is a prerequisite for successful basis material decomposition. Registered image volumes were saved as *.TIF sequences.

2.8.2 | Basis material decomposition

All dual-energy scans were subject to a basis material decomposition to derive material fractions of the casting agent versus the specimen tissue. Values for the

decomposition matrix (for details, see Ref. [40]) were derived from joint dual-energy profiles of the two scans.[42] Separate reference scans were not required, because the casting agent and the biological tissues are well separated and there is no anatomical overlap among these fractions. Regions of interest were defined in image pairs, and slope and intercept were derived using the FIJI ImageJ[70] tool *colocalization threshold*. Slope and intercept values as well as values of the decomposition matrix are summarised in Table S5. For all acquired scans, the pseudo-CT number of the casting agent was higher in the high-energy scan (slope > 1), whereas the pseudo-CT number of the biological tissues (both mineralised tissue and B-PTA stained soft tissue) was higher in the low-energy scan (slope < 1). This is related to the *k*-edges of the casting materials and the chosen energy pairs. The custom Matlab tool DECTDec (https://github.com/microDECT/DECTDec; for a detailed description, see Ref. [42]) was used to extract three material fractions from the two scanning energies as described by Ref. [40]. The extracted material fractions were saved as *.TIF sequences. A third background fraction ('water') was extracted,[42] but this channel is not discussed or depicted in the results of the present work as it contained no information relevant to the main aim of the present work.

2.9 | Visualisation of microDECT data

After material fractions were extracted, data were re-imported into Amira (FEI Visualization Sciences Group, part of Thermo Fisher Scientific, Mérignac Cédex, FR, versions 2019–2022) and saved in *.AM format. For 3D visualisation, we used the tool *Volume Rendering*. Extracted material fractions were visualised by monochrome renderings; in addition, *Multi-channel fields* were used to create two colour (green/magenta) renderings. For Supporting Information figures, we also used two colour volume renderings (grey/red). Single-slice images (monochrome and multichannel) were created either in Amira of FIJI ImageJ. Maximum intensity projections (monochrome and multichannel) were created in FIJI ImageJ. Semi-naturalistic volume renderings were created for selected datasets using Drishti.[71] Information on the software used is summarised in Table S6. The dynamic range in extracted material fractions can be very large, especially for fractions that include mineralised tissue and B-PTA-stained soft tissue. For every figure, histogram settings were adapted by linear scaling (no gamma function) to show also low-contrast details of the scan. Thus, some areas (such as bone) may appear oversaturated in the figures, but this is only a matter of display (histogram settings), and in the raw 16 bit material fractions, the tissues are not oversaturated.

2.10 | Exemplary strategies for microDECT data segmentation and analysis

The Amira *Segmentation Editor* was used for threshold segmentation based on extracted material fractions. Alternatively, we used the Amira *Correlation histogram* of the registered and resampled low- and high-energy scans to draw regions of interest for different materials that were then converted to label masks. Based on segmented label data, we used the *Generate Surface* tool to create polygon models, which were then smoothed (*Smooth Surface*) and rendered (*Surface View*). In one scan of the mouse skull and brain, we semi-manually segmented the cerebellum from the HA + B-PTA material fraction and then used a Boolean operation to only analyse vasculature that lies inside the cerebellum region. The *Material statistics* tool was used to measure volume of the cerebellum and vasculature inside the cerebellum.

3 | RESULTS

3.1 | Perfusion quality

Preview scans were acquired to check in which body regions the vascular network was filled with the casting agent. The used protocol included formalin perfusion prior to manual perfusion with the casting agent. Formalin perfusion yields good tissue fixation but also causes hardening of the vessel walls, potentially compromising the permeability of small capillaries. We found the µAngiofil casting agent in large parts of the veinous system, including the large veins of head and kidney (Figure S1), suggesting that the casting agent successfully passed the capillary bed in these body regions. High-resolution scans confirmed the filling of capillaries with µAngiofil contrast agent (Figure S2). The intensity of the filled vasculature was homogenous in most vessels, which suggests that the µAngiofil contrast agent was homogeneously mixed with the polyurethane carrier and the hardener; however, we also observed some areas where this was not the case, indicating that the mixing procedure was not optimal. Heterogenous attenuation was observed in some large veins, and in addition, unmixed portions of the µAngiofil contrast agent remained as liquid droplets that appeared as highly attenuating spots in the scan (Figure S1). This shortcoming in perfusion quality, however, did not impair the development of counterstaining and microDECT imaging protocols.

3.2 | MicroDECT imaging of vasculature and mineralised tissue

MicroDECT imaging of µAngiofil perfused vasculature versus mineralised tissue is demonstrated on a mouse

head sample (*sample ID 2-1-1*). The x-ray attenuation properties of iodine allowed an effective spectral separation of μAngiofil-perfused vasculature from mineralised tissue. Spectral contrast was already evident in the overlay image of 40 and 80 kVp slices (Figure 1A). Basis material decomposition was used to isolate well-separated material fractions (Figure 2, Movie S1). In addition to the overview microDECT scan of the entire head (13.94 μm isotropic voxel size, Figure 2A), we acquired higher resolution region of interest (ROI) scans (interior tomographies) from the posterior part of the skull (7.81 μm isotropic voxel size, Figure 2B) as well as the nasal cavity (2.24 μm isotropic voxel size, Figure 2C). The display as a two-colour overlay image shows the advantages of microDECT over single-energy data, exemplified in the inner ear region (Figure 2B). Vessels such as the stapedial artery are in close contact with the bone tissue and thus often hard to distinguish and analyse in the single-energy scan (Figure 2B, left), whereas they can be clearly identified in the overlay of the extracted material fractions (Figure 2B, right). The quality of spectral separation was high in all acquired microDECT scans, including even minute morphological features such as the thin bony nasal turbinates and the capillaries of the olfactory epithelium (Figure 2C). The extracted material fractions could be readily used for two-channel volume rendering (Figure 2D, right). Semi-naturalistic rendering settings were applied to create visualisations of the complex anatomical relationships between skeleton and vasculature (Figure 3). MicroDECT data did not only allow these visualisations, but it also facilitated automated segmentation of vessels that are in direct vicinity of bone tissue. Figure 4 depicts two approaches to segment microDECT data, applicable for larger and medium-sized blood vessels. The first approach used basis material decomposition followed by threshold segmentation of the two material fractions. The second approach used direct ROI-guided segmentation based on the joint dual-energy histogram. For the imaged ROI (7.81 μm voxel size), the joint dual-energy histogram approach enabled a slightly more complete segmentation of the vasculature and resulted in an 11.9% larger vasculature volume (62.65 mm^3) compared to the thresholding approach (55.97 mm^3). Both segmentation approaches enabled a largely complete segmentation of larger and medium-sized vessels up to a diameter of ~30 μm (~4 voxels). However, the smallest visible vessels in the dataset with a diameter between ~15 and 30 μm (2–4 voxels) were not captured by either approach.

In addition to the mouse head, microDECT imaging of μAngiofil versus mineralised tissue was performed on a mouse forepaw (*sample ID 2-2-1*) (Figure S2) and a piece of mouse tail (*sample ID 2-3-1*) (Figure S4).

3.3 | MicroDECT imaging of vasculature and soft tissue

MicroDECT imaging of μAngiofil-perfused vasculature versus B-PTA-stained soft tissue is demonstrated on mouse brain (*sample ID 2-1-4*) imaged at 5.42 μm isotropic voxel size. The attenuation properties of iodine (*k*-edge = 33.17 keV) and tungsten (*k*-edge = 69.52 keV) provide high spectral contrast when imaged using a 40 kVp/80 kVp energy pair. Spectral contrast was already evident in the overlay image of 40 and 80 kVp slices (Figure 1B). The basis material decomposition yielded an effective separation of the μAngiofil and B-PTA material fractions, which allowed to put the vasculature into context with general brain anatomy (Figure 5A,B). Maximum intensity projections (1 mm thick slices) allowed to visualise larger aspects of vasculature in the context of different brain regions (Figure 5C). Semi-naturalistic volume renderings allow to simultaneously visualise cerebral vasculature and brain tissue in 3D (Figure 6).

3.4 | MicroDECT imaging of vasculature, bone and soft tissue

MicroDECT imaging of μAngiofil-perfused vasculature versus mineralised tissue and B-PTA-stained soft tissue is demonstrated again on the mouse head sample. The attenuation properties of calcium (*k*-edge = 4.04 keV) and tungsten (*k*-edge = 69.52 keV) provided no measurable spectral contrast when imaged with a 40 kVp/80 kVp energy pair. Thus, bone and PTA-stained soft tissue were merged into a single-material fraction that spectrally separated well from the μAngiofil material fraction. This was readily visible in the μAngiofil perfused and B-PTA-stained mouse head sample (*sample ID 2-1-2*). Basis material decomposition allowed to effectively separate HA-mineralised tissue and B-PTA-stained soft tissue from μAngiofil perfused vasculature, as shown in slices (Figure 7A) and maximum intensity projection thick slices (Figure 7C). Removal of lower jaw, tongue, masseter muscles, eyes, and salivary glands (*sample ID 2-1-3*) prior to imaging with a smaller isotropic voxel size (5.64 μm) improved the signal-to-noise ratio and resolution in the brain and its vasculature (Figure 7B). The combined HA plus B-PTA material fraction had a huge dynamic range, because x-ray attenuation in mineralised tissue was much higher compared to the B-PTA-stained soft tissue. This allowed to split the intensity histogram of this material fraction into two components. The lower intensity component represented the B-PTA-stained soft tissue, whereas the higher intensity component represented the mineralised

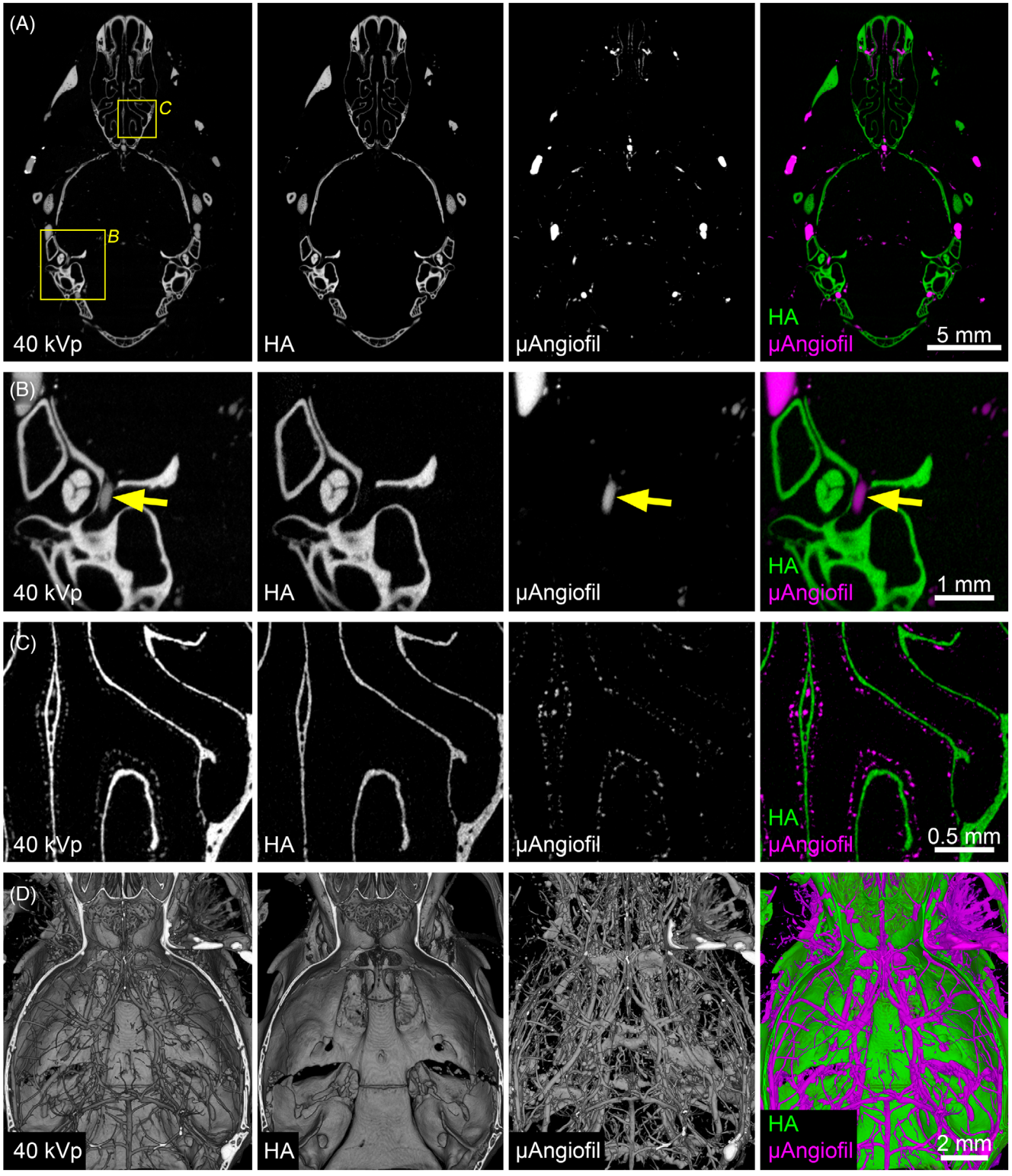

FIGURE 2 Microscopic dual-energy CT (microDECT) imaging of the head of an adult mouse after μAngiofil perfusion (*sample ID 2-1-1*). (A) Horizontal section of the mouse head, imaged with 13.94 μm isotropic voxel size. The left figure shows a single slice from the 40 kVp scan. The two middle images show slices from the hydroxyapatite (HA) and μAngiofil material fractions, which were calculated based on basis material decomposition. The right image shows a colour overlay of the two material fractions. (B) Region of interest scan (interior tomography) showing the inner ear region, imaged with 7.81 μm isotropic voxel size. Arrows indicate the stapedial artery. (C) Region of interest scan (interior tomography) showing the nasal cavity, imaged with 2.24 μm isotropic voxel size. With this scan resolution, a high level of detail is achieved both for bony structures and the capillaries of the olfactory mucosa. (D) Volume renderings of the entire field of view of the 7.81 μm 40 kVp scan, the HA and μAngiofil material fractions, and the colour overlay of the two material fractions.

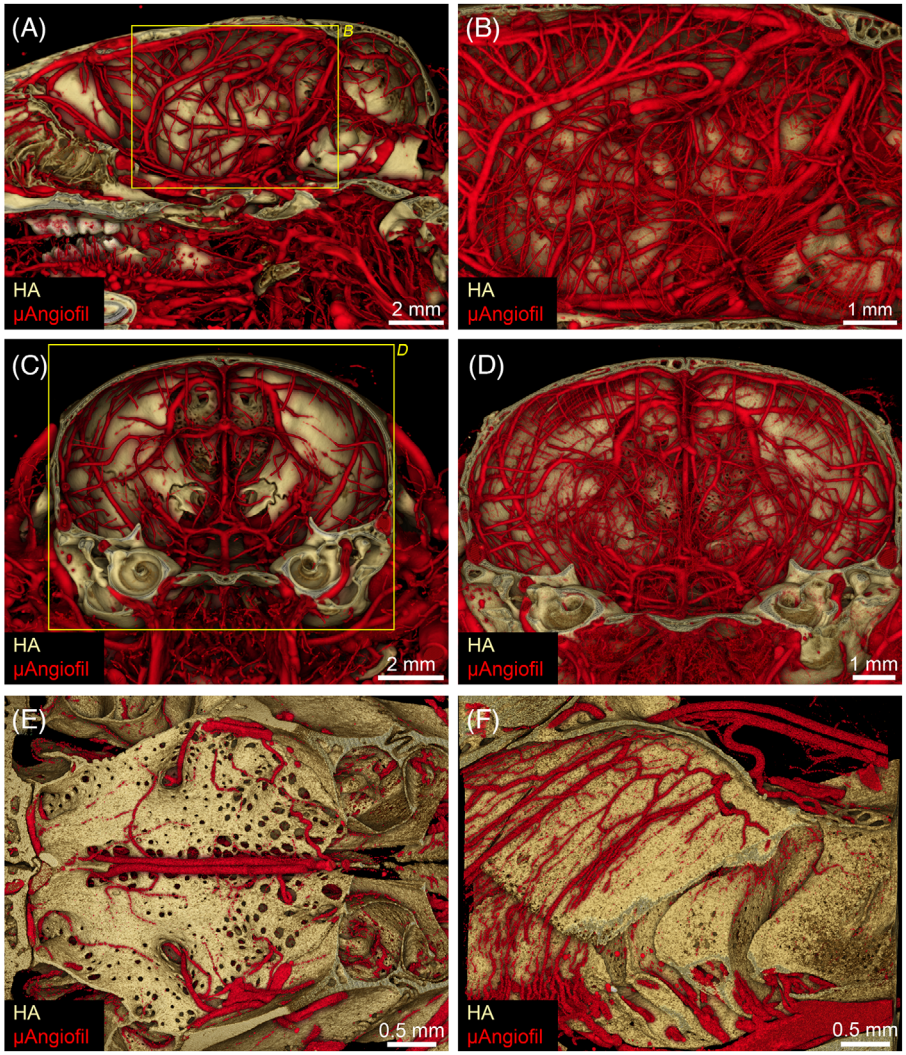

FIGURE 3 Semi-naturalistic 3D volume renderings based on microscopic dual energy CT (microDECT) imaging of the head of an adult mouse after μAngiofil perfusion (*sample ID 2-1-1*). The hydroxyapatite (HA) material fraction was rendered with an ochre transfer function, whereas the μAngiofil material fraction was rendered with a red transfer function. (A) Lateral view of the head virtually cut in a parasagittal plane. Head imaged with 13.94 μm isotropic voxel size. This scan resolution allows to display the larger vessels of the head. (B) Lateral view of the head, imaged with 7.81 μm voxel size. This scan resolution allows to display much smaller vessels compared to (A). (C) Posterior view of the head virtually cut in a coronal plane. Head imaged with 13.94 μm isotropic voxel size. (D) Posterior view of the head, imaged with 7.81 μm isotropic voxel size. (E) Dorsal view on the lamina cribrosa, imaged with 2.24 μm voxel size. (F) Lateral view on the nasal cavity, imaged with 2.24 μm voxel size.

tissue (Figure 8A). Thus, segmentation of bone was possible even in the presence of B-PTA-stained soft tissue. Using this approach for the mouse head, one microDECT scan yielded information on the skull, on brain anatomy and on vasculature (Figure 8B). When compared to the μAngiofil-filled, B-PTA-stained and isolated mouse brain (Figure 5), signal-to-noise ratio in the brain was slightly lower in the presence of bone (Figure 7). However, for the mouse brain, this approach had two clear advantages. First, vasculature could be depicted and analysed not only with reference to brain regions (or, more generally, soft tissue anatomy) but also with reference to skull morphology (or, more generally, skeletal features) (Figure 9). Second, vasculature could be analysed without the introduction of any preparatory distortions such as cracks in brain tissue or distortions/displacements of vessels that lie in the close vicinity of skull bone, thus facilitating a variety of quantitative analyses. As one example, we semi-manually segmented one brain region (cerebellum). After creating a threshold segmentation of vasculature, we used a Boolean operation to crop only vasculature inside the cerebellum, which we then used to calculate the volume of vasculature inside the cerebellum (Figure 10).

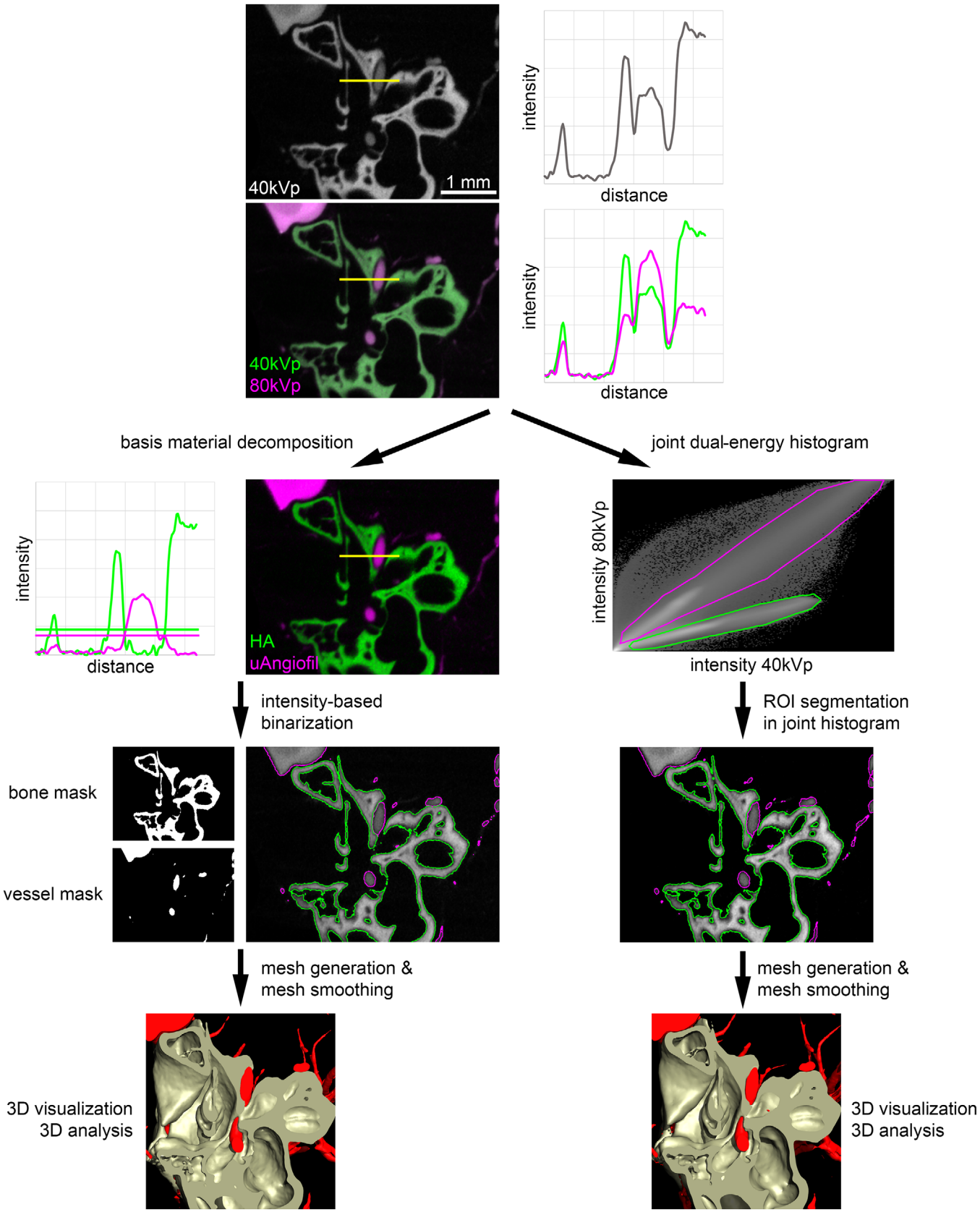

FIGURE 4 Two segmentation strategies for microscopic dual-energy CT (microDECT) scans to simultaneously visualise mineralised tissue and μAngiofil-perfused vasculature (*sample ID 2-1-1*). In single-energy datasets such as the displayed 40 kVp scan, the vasculature cannot be separated from mineralised tissue based on intensity thresholding because the histograms of bone tissue and perfused vessels partly overlap (top image and line profile). In contrast, microDECT datasets such as the displayed 40 kVp/80 kVp scan and line profile provide

In addition to the mouse head, microDECT imaging of µAngiofil versus bone and B-PTA-stained soft tissue was successfully tested in a mouse forepaw (Figure S5) and a piece of mouse tail (Figure S6).

4 | DISCUSSION

4.1 | Merits of the presented workflow

MicroCT imaging of specimens perfused with an x-ray dense casting agent has proven to be an adequate and valuable tool for studying various vascular disorders. Although the quantitative analysis of the casting agent alone can provide sufficient information, the visualisation of conventional vessel perfusion samples is subject to two limitations.

A first concern is the analysis of perfused vasculature in the direct vicinity of mineralised tissue. Using an energy range usually used in laboratory-based microCT imaging of small ex vivo biopsy specimens (~40–90 kVp), the histograms of mineralised tissue and casting agents may frequently overlap, thus making intensity-based segmentation challenging. Higher scan energies[72] or very high concentrations of contrast agent[15] can be used for improving casting agent contrast with reference to bone, but segmentation of small vessels may still be difficult due to, for example, partial volume effect. Using microDECT, a clear spectral contrast of vasculature versus mineralised tissue can be achieved (Figures 1 and 2), which can be utilised in image segmentation, facilitating thresholding of material fractions (Figure 4), segmentation based on the joint histograms of the registered and resampled low and high-energy scans (Figure 4), singular value decomposition of the material fractions,[42] machine learning–based pixel classification of the registered and resampled low- and high-energy scans[42] or even deep learning–based segmentation. We tested two segmentation approaches—thresholding of material fractions and segmentation based on the joint histograms—on a dataset with mineralised tissue and µAngiofil-filled vessels (Figure 4). Both approaches provided comparable results and largely complete segmentation of µAngiofil-filled vessels up to a vessel diameter of ~4 voxels in the binary segmentation mask (i.e. ~30 µm, voxel size = 7.81 µm). Although generally comparable, some differences were found between the two segmentation strategies. The joint histogram approach allowed a more complete segmentation of the vasculature (11.9% larger vessel volume compared to the thresholding approach). The joint histogram approach is also simpler, as it is performed directly on the registered scans and does not rely on the step of decomposing the material fractions. For many segmentation tasks, the joint histogram approach is therefore the right choice, as it provides satisfactory results for larger and medium-sized vessels. When the smallest visible vessels in the datasets (2–4 voxels diameter) are the focus of interest, other segmentation tools are needed. The use of deep learning convolutional neural networks (CNNs) seems to be most promising, as when using CNNs, the successful detection of vessels does not only depend on intensity but also on the object shape and the object neighbourhood.

The second limitation in the imaging of perfused samples concerns the typical lack of reference information on soft tissue. Previous works have pointed this out and presented options for adding soft tissue information. Hlushchuk et al.[21] dehydrated muscle samples and added a thin paraffin layer in order to add information about muscle fibres. Rosenblum et al.[73] presented an iterative workflow for imaging the murine cranial vasculature, where the samples are imaged three times (Scan 1: after perfusion, Scan 2: after decalcification, Scan 3: after soft tissue-counterstaining). However, the latter approach uses non-rigid registration procedures, which are error-prone and cannot compensate for all sample artefacts such as shrinkage and tissue deformation that occur during the sample preparation procedure; thus, this iterative workflow has limitations when it comes to fine details of vasculature and soft tissue morphology. Bhargava et al.[74] described a multimodal pipeline that uses MRI for providing soft tissue reference data (e.g. the mouse brain) in vascular phenotyping pipelines. However, this multimodal approach requires a specific MRI contrast agent and another image acquisition step at the MRI scanner, and even more critically, the soft tissue MRI data have typically much lower spatial resolution than the microCT data. When it comes to adding soft tissue reference information on mesoscopic level to support interpretation and analysis

sufficient spectral information to allow intensity-based segmentation of large- and medium-sized blood vessels. Two segmentation strategies are shown. The left panel shows the basis material decomposition approach, in which two material fractions (hydroxyapatite [HA] and µAngiofil channels) are calculated. These channels can be used for threshold segmentation and subsequent 3D visualisation and analysis. The right panel shows the joint dual-energy histogram approach, which is simpler and more straightforward. Regions of interest are directly defined in the joint histogram of the 40 and 80 kVp scans, then converted to segmentation masks and used for subsequent 3D visualisation and analysis. In this example, the two approaches led to similar results. As previously shown,[42] other segmentation approaches such as singular value decomposition or machine learning–based pixel classification can also be used for microDECT datasets.

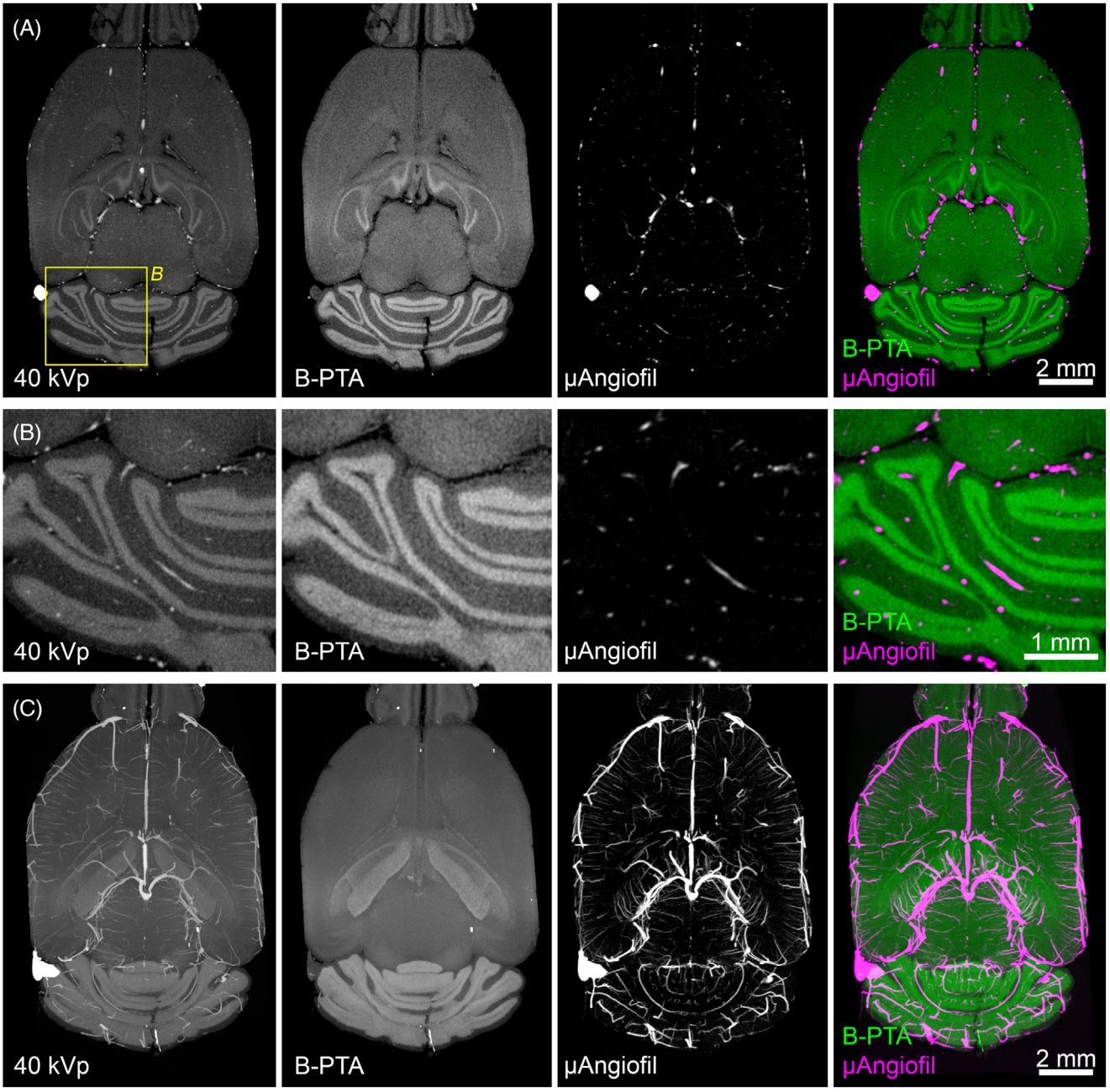

FIGURE 5 Microscopic dual-energy CT (microDECT) imaging of the brain of an adult mouse after µAngiofil perfusion and counterstaining with Sorensen-buffered phosphotungstic acid (B-PTA) (*sample ID 2-1-4*). (A) Horizontal section of the mouse brain, imaged with 5.42 µm isotropic voxel size. The left figure shows a single slice from the 40 kVp scan. The two middle images show slices from the B-PTA and µAngiofil material fractions, which were calculated based on basis material decomposition. The right image shows a colour overlay of the two material fractions. (B) Magnified region of interest (cerebellum) of the same scan. (C) Maximum intensity projection thick slices (1 mm) of the 40 kVp scan, the B-PTA and µAngiofil material fractions, and the colour overlay of the two material fractions, showing a larger anatomical aspect of the perfused vasculature compared to the single slices.

of vascular phenotypes, we think that the approach presented is simpler and more straightforward. We utilise a spectral microDECT imaging approach of vascular casting specimens in which soft tissue is counter-stained with an x-ray dense contrast agent (B-PTA). The vascular system and the soft tissue are imaged in one dual-energy scan. This removes the necessity of either adding another imaging modality (MRI) or using non-rigid registration procedures for different datasets originating from iterative sample processing. The novel counterstaining protocol reported here using B-PTA solution provides excellent spectral contrast, leaves the perfused vessels intact and

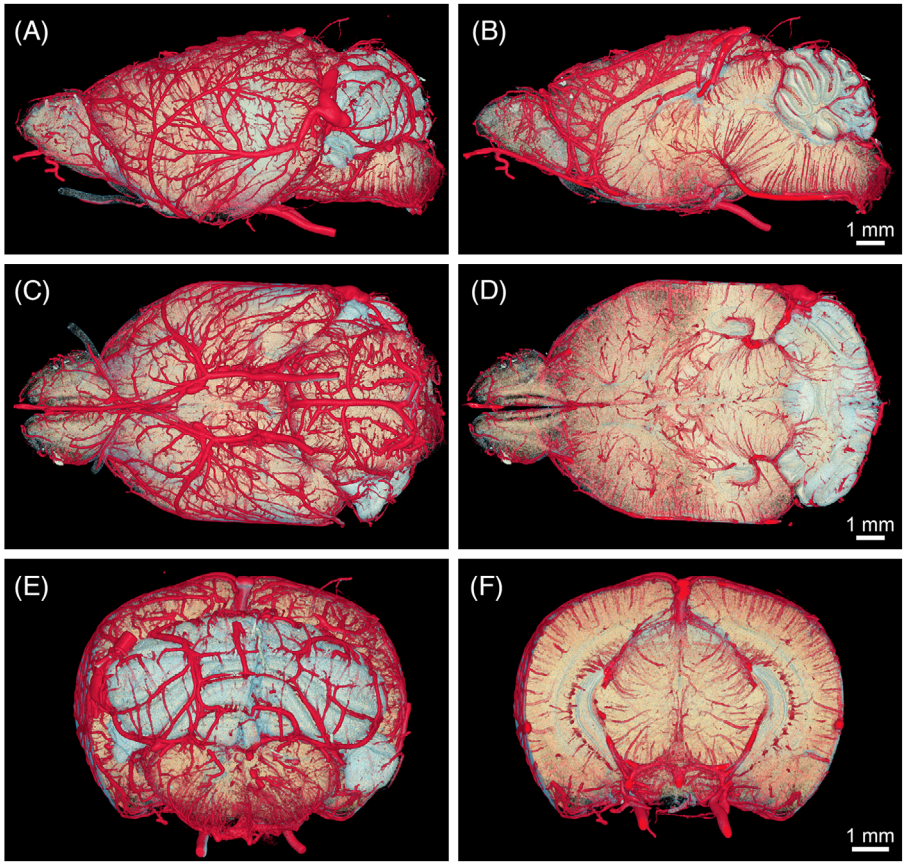

FIGURE 6 Semi-naturalistic 3D volume renderings based on microscopic dual-energy CT (microDECT) imaging of the brain of an adult mouse after µAngiofil perfusion and counterstaining with Sorensen-buffered phosphotungstic acid (B-PTA) (*sample ID 2-1-4*). MicroDECT scan acquired with 5.42 µm isotropic voxel resolution. The B-PTA material fraction was rendered with a yellowish to blueish transfer function, wheras the µAngiofil material fraction was rendered with a red transfer function. (A) Lateral view of the brain. (B) Lateral view of the brain virtually cut in a parasagittal plane. (C) Ventral view of the brain. (D) Ventral view of the brain virtually cut in a horizontal plane. (E) Posterior view of the brain. (F) Posterior view of the brain virtually cut in a coronal plane.

causes no visible sample shrinkage (see below). Structural features of soft tissue can serve as a reference for the analysis of vasculature. To highlight a potential application, we semi-manually segmented the cerebellum as a mask for measuring the volume of vasculature within the cerebellum at the given scan resolution (Figure 10). This showcases how soft tissue reference information can be used for Boolean operators in order to derive more specific information on vasculature. As an example, a segmented 3D brain atlas[75] could be registered to datasets and used to automatically extract vasculature volume at a given scan resolution for all brain regions.

Further, microDECT could be used for vascular analysis with reference to both mineralised and stained soft tissue (Figures 7–9). Due to the high dynamic range of extracted 16 bit material fractions, and the lower attenuation in B-PTA-stained soft tissues compared to B-PTA-stained mineralised tissues, the combined calcium and tungsten signal (HA/B-PTA material fraction) can be split into a soft tissue and a mineralised tissue component (Figure 8). This offers multiple opportunities for an analysis similar to the rationale presented by Rosenblum et al.,[73] but without requiring iterative sample processing, repeated scanning and non-rigid (i.e. elastic and deformable) image volume registration procedures.

4.2 | Applicability of the presented microDECT imaging methods to other vascular casting contrast agents such as Micropaque barium sulphate

It was our aim to evaluate the applicability of spectral microDECT imaging procedures also for the vascular casting agent barium sulphate.[17,76–80] The x-ray attenuation properties of barium (*k*-edge = 37.44 keV) also allowed the spectral separation of Micropaque-perfused vasculature from mineralised tissue (Figure S7A) and PTA counter-stained soft tissues (Figure S7B) when using a 45 kVp/80 kVp energy pair. Separation of

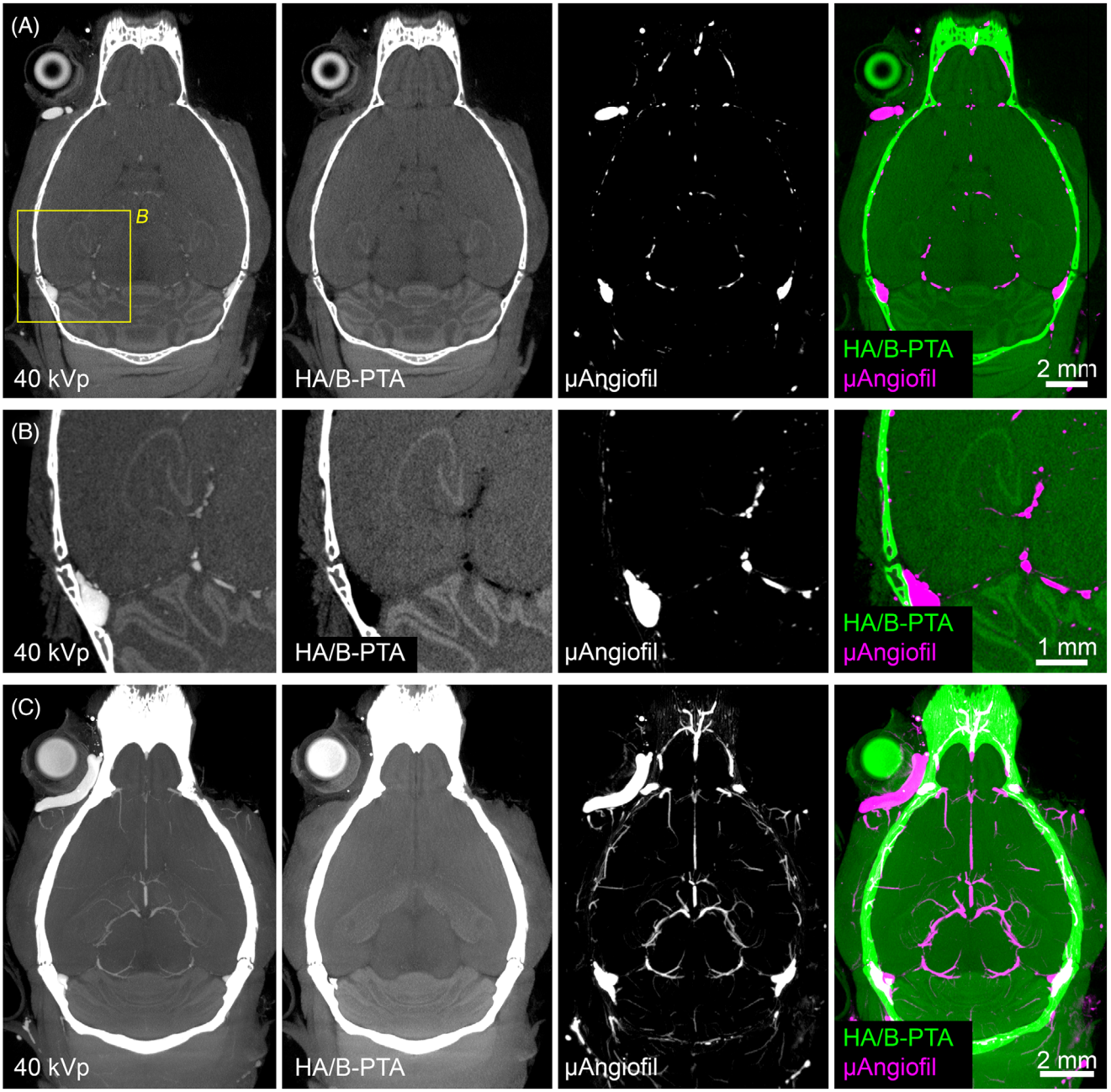

FIGURE 7 Microscopic dual-energy CT (microDECT) imaging of the head of an adult mouse after µAngiofil perfusion and counterstaining with Sorensen-buffered phosphotungstic acid (B-PTA) (*sample IDs 2-1-2* and *2-1-3*). Note that prior to B-PTA staining, one eye was removed, and the skin was peeled off to allow better penetration of the B-PTA solution. For the higher resolution region of interest scan (B), the lower jaw, tongue and masseter muscle were removed prior to imaging. Although contrast and signal-to-noise ratio were slightly lower when imaging the brain and its vasculature in the intact skull, the brain was free of artefacts such as cracks in the brain tissue or olfactory bulbs, and vasculature that is in the direct vicinity of the skull could be imaged without distortions introduced by sample preparation (compare to isolated brain, Figure 5). (A) Horizontal section of the mouse head, imaged with 13.94 µm isotropic voxel size (sample ID 2-1-2). The left figure shows a single slice from the 40 kVp scan. The two middle images show slices from the hydroxyapatite (HA) + B-PTA and µAngiofil material fractions, which were calculated based on basis material decomposition. The right image shows a colour overlay of the two material fractions. (B) Region of interest scan (interior tomography) showing the hippocampus region and cerebellum, imaged with 5.64 µm isotropic voxel size (sample ID 2-1-3). (C) Maximum intensity projection thick slices (1 mm) of the 13.94 µm isotropic voxel size 40 kVp scan, the HA + B-PTA and µAngiofil material fractions, and the colour overlay of the two material fractions, showing a larger anatomical aspect of the perfused vasculature compared to the single slices (sample ID 2-1-2).

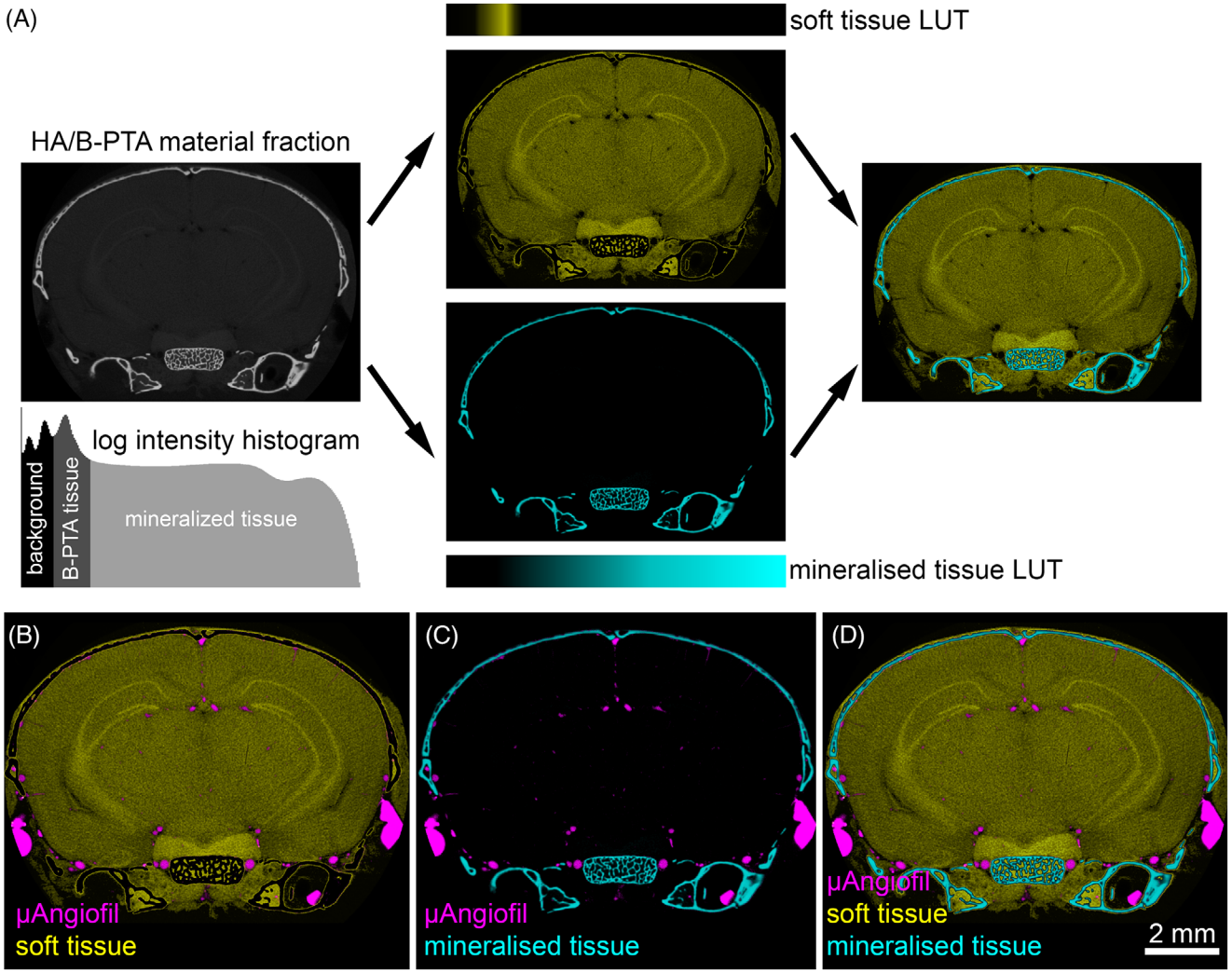

FIGURE 8 Visualisation of microscopic dual-energy CT (microDECT) data of a mouse head after µAngiofil perfusion and counterstaining with Sorensen-buffered phosphotungstic acid (B-PTA) (*sample ID 2-1-3*). (A) During the basis material composition, hydroxyapatite (HA) (mineralised tissue) and B-PTA (stained soft tissue) signals are merged into a single-HA/B-PTA material fraction due to the similar spectral properties when imaged at a 40 kVp/80 kVp energy pair. However, the dynamic range of this material fraction is large and allows separation of mineral and soft tissue based on intensity values. False-colour look up tables (LUT's) can be specifically designed to fit the intensity ranges of mineralised tissue (cyan) and PTA-stained soft tissue (yellow). (B–D) The µAngiofil material fraction can then be jointly displayed and analysed with one or both compounds of the HA/B-PTA material fraction.

Micropaque-perfused vasculature from mineralised tissue allowed effective basis material decomposition (Figure S8) and dedicated transfer functions allowed 3D visualisation of the vasculature within the context of bone in a mouse head sample (Figure S9). Similarly, Micropaque-perfused samples could be counter-stained with an ethanolic PTA solution and imaged using a 45 kVp/80 kVp energy pair. Also here, the basis material decomposition yielded an effective separation of the Micropaque and PTA material fractions (Figure S10).

Regarding perfusion quality, we observed differences between µAngiofil- and Micropaque-perfused animals. In the latter, in our hands, most parts of the veinous system were empty, suggesting the contrast agent failed to pass the majority of capillaries. This pattern was observed in several areas of the body, including the head and kidneys (Figure S1). Many large- and medium-sized arteries were filled. This allowed us to develop suitable spectral imaging protocols, which was the aim of the present study, and no effort was put on improving barium sulphate perfusion quality. Thus, limited perfusion quality must not be seen as an absolute statement about the limited ability of barium sulphate crystals to pass capillaries, as several previous studies have demonstrated the suitability of barium sulphate particles for imaging of capillaries.[15,79]

Moreover, other contrast agents have been shown to be suitable for the microscopic ex vivo study of vascular anatomy, like the lead-based Microfil[25] and the

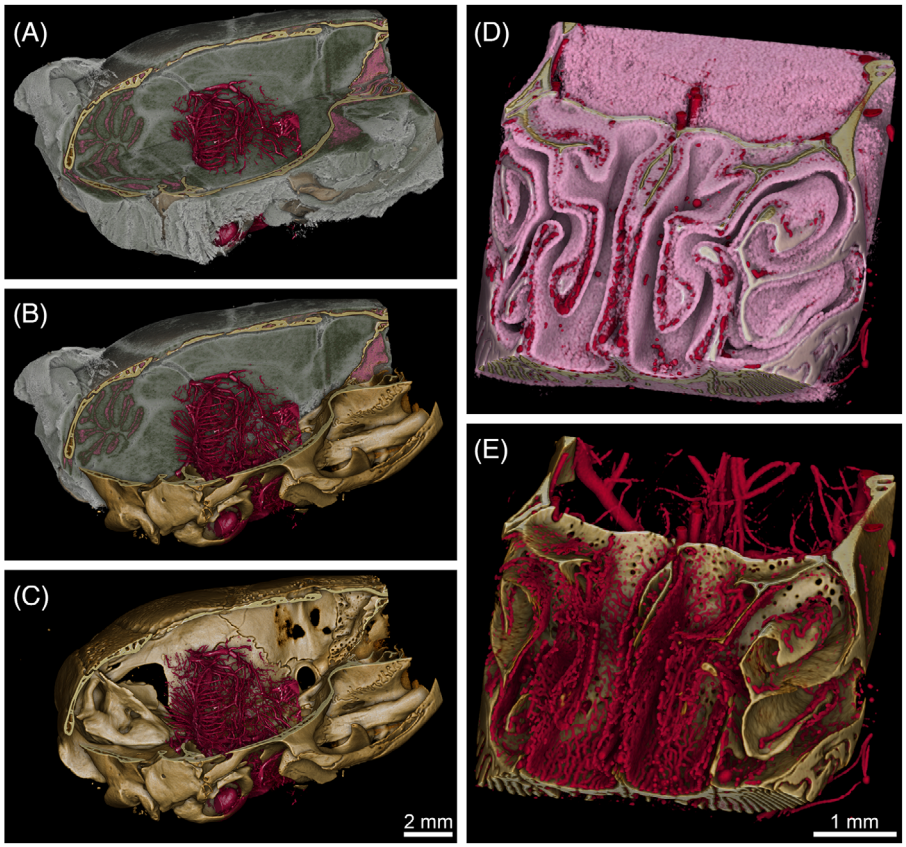

FIGURE 9 3D renderings of microscopic dual-energy CT (microDECT) data of the head of an adult mouse after μAngiofil perfusion and counterstaining with Sorensen-buffered phosphotungstic acid (B-PTA) (*sample ID 2-1-2*). As demonstrated in Figure 8, the dynamic range of the hydroxyapatite (HA)/B-PTA material fraction allows to split the two components (mineralised tissue vs. B-PTA-stained soft tissue) by means of intensity-based transfer functions. (A) 3D rendering of a mouse skull scanned with 7.81 isotropic voxel size, rendered with three transfer functions (μAngiofil material fraction = red, mineralised tissue compound = ochre, B-PTA-stained soft tissue = whitish/greenish/pinkish). Different regions of interest (ROIs) rendered for the three transfer functions. The ROI of the μAngiofil transfer function was set to show the right hippocampus region. (B) Same view as in A, but smaller ROI chosen for the B-PTA-stained soft tissue transfer function. (C) Same view as in (A) and (B), but only two transfer functions rendered (μAngiofil material fraction, mineralised tissue compound). The B-PTA-stained soft tissue is not displayed. (D) 3D rendering of a mouse nasal cavity scanned with 2.24 isotropic voxel size, rendered with three transfer functions (μAngiofil material fraction = red, mineralised tissue compound = ochre, B-PTA-stained soft tissue = pinkish). (E) Same view as in (D), but only two transfer functions were rendered (μAngiofil material fraction, mineralised tissue compound). The B-PTA-stained soft tissue is not displayed.

novel bismuth-based Vascupaint.[14] However, both contrast agents contain elements with a high atomic number (lead = 82, bismuth = 83) and thus high *k*-edges (lead = 88.0 keV, bismuth = 90.5 keV). Such high *k*-edges complicate dual-energy microDECT imaging with conventional lab-based microCT equipment, as the mean photon energy of the high-energy scan cannot be placed above the *k*-edge of the contrast agent, making spectral separation from mineralised tissue—although possible when using very high scan energies[24]—less easy and efficient.

4.3 | Soft tissue staining with B-PTA

While developing presented microDECT imaging workflows, it was our aim to find a simple and robust method for counterstaining soft tissue in the presence of the vascular casting agents μAngiofil and Micropaque. With Micropaque, we used 1% (w/v) PTA in 70% ethanol as used before.[48,54] With μAngiofil, the same protocol resulted in the formation of a variety of artefacts in the casted vessels. For example, dehydration in 70% ethanol for 48 h caused the disintegration of the homogenous mixture of contrast agent and polyurethane polymer, forming droplets of highly stained μAngiofil contrast agent in a weakly stained matrix of casting agent (Figure S11A,B). Using PTA in water instead of ethanol provided high soft tissue contrast. However, PTA contrast was found in the periphery of polyurethane polymers (Figure S11C,D). This suggests binding of PTA to the polymer in acidic aqueous environment, complicating the spectral separation of vasculature

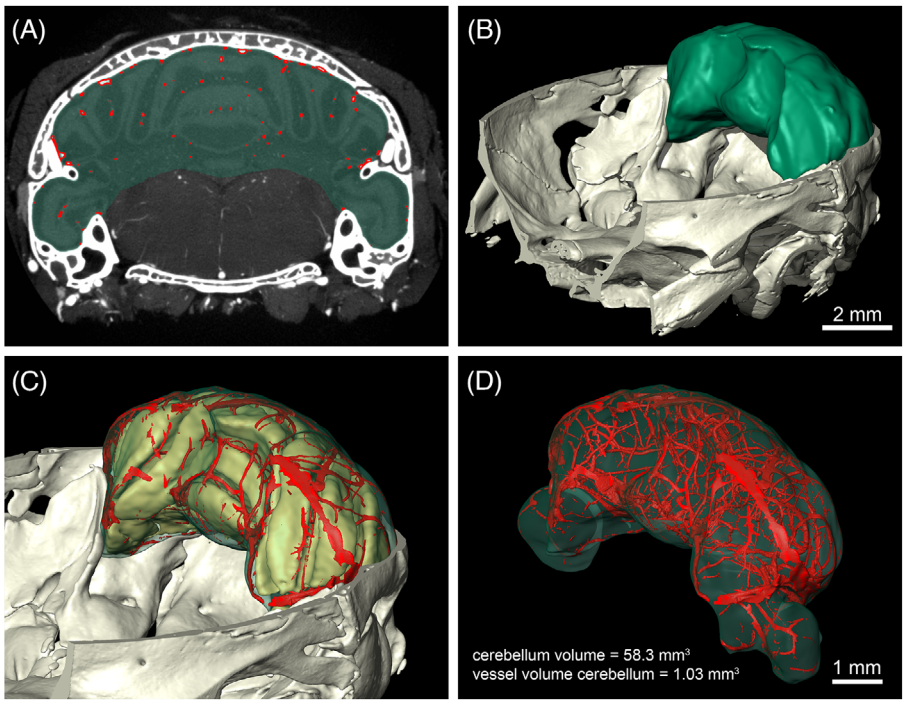

FIGURE 10 Options for quantitative analysis of microscopic dual-energy CT (microDECT) data and simultaneous visualisation of mineralised tissue, Sorensen-buffered phosphotungstic acid (B-PTA)-stained soft tissue, and μAngiofil-perfused vasculature (*sample ID 2-1-3*). (A) The B-PTA stain allows to segment brain regions. Segmented brain regions can then be used as masks for the segmentation of vasculature. In this example, vessels (red mask) inside the cerebellum (green mask) were segmented automatically based on intensity thresholding. Subsequently, all vessels outside the cerebellum were removed by a Boolean operation. (B) 3D visualisation of the cerebellum and the skull. (C) Semi-transparent visualisation of the cerebellum (green), with the granular layer rendered yellowish and the vasculature red. (D) Transparent visualisation of the cerebellum showing the segmented vasculature. Note that the presented segmentation does not include smallest vessels.

and soft tissue iodine and tungsten during basis material decomposition.

We finally ended up with using a 2.5% (w/v) solution of PTA in Sorensen buffer, which seemed to perfectly combine the four most critical properties in the context of using a contrast agent as a counterstain for μAngiofil. First, on a mesoscopic scale, it leaves the μAngiofil-perfused vasculature unaffected. Second, the tungsten of the PTA provides optimal spectral contrast against μAngiofil (see Handschuh et al.[42] on spectral separation of iodine and tungsten). Third, B-PTA apparently yields only minimal tissue shrinkage, unlike the effects obtained by using aqueous PTA solutions for staining tissues, including brain.[81] This aspect is important as tissue shrinkage can impair the analysis of soft tissue. In the context of analysing vasculature with reference to the skull and brain, shrinkage of the brain is typically observed with conventional staining solutions, resulting in an artificial gap between brain and skull.[73] Fourth, B-PTA provides sufficient but still comparatively low soft tissue x-ray attenuation. This aspect is especially critical because, in case, that attenuation in counter-stained soft tissue would be too strong, this would impair the spectral detection and segmentation of small vessels due to partial volume effect.

To our knowledge, this paper is the first to report the use of B-PTA solution for staining soft tissues for the purpose of microCT imaging. However, the rationale for using a Sorensen-buffered staining solution is not new but comes from the seminal paper of Dawood et al.,[69] which demonstrated that soft tissue shrinkage observed after staining in aqueous Lugol's iodine potassium iodide (I_2KI) can be almost eliminated when using a Sorensen-buffered solution (B-Lugol). They showed that shrinkage occurs primarily because of the acidification of the staining solution. When using the B-PTA contrast protocol, we similarly observed reduced or eliminated tissue shrinkage. Therefore, it is possible that the higher pH of 6.28 in the buffered 2.5% (w/v) B-PTA solution compared to pH 1.54 in a 1% (w/v) aqueous PTA solution is the cause for this valuable improvement. Moreover, staining in B-PTA prevented the PTA molecules from binding to the outer zone of the polyurethane carrier as seen in aqueous PTA solution (Figure S11B).

Although B-PTA provides good staining results and a reliable spectral separation from the perfusion casting

agent μAngiofil, it seems likely that the counterstaining of samples perfused with μAngiofil can be further improved. Promising candidates for this purpose are Wells–Dawson polyoxometalates such as the hafnium-substituted Wells–Dawson polyoxometalate, which has similar spectral x-ray properties and soft tissue contrast but has the advantage of much faster soft tissue diffusion compared to PTA.[82,83]

4.4 | Limitations of the datasets presented and possible future workflow improvements

The present workflow can be used to image vasculature at micron resolution in mineralised and non-mineralised tissue in uncleared samples up to the size of an entire mouse head. Thus, it represents an easy and straightforward approach for gaining quantitative information about the vascular system. Samples are left intact by microCT scanning, hence can be used for downstream histological immunochemical processing and analysis, provided compatibility of protocols.

Despite these advantages, the datasets presented here show some limitations. The first limitation relates to the quality of perfusion. As stated in Section 1, the present work focused on establishing counterstains and microDECT image protocols, and no particular emphasis was placed on achieving the best possible vascular perfusion result. Perfusion fixation with 4% formalin yields a high quality of tissue fixation but also causes a stiffening of vessel walls, potentially complicating the passage of the contrast agent through capillaries. The original publications introducing μAngiofil as a casting agent did not use formalin perfusion fixation prior to vascular casting.[21,22] Thus, the quality of perfusion could be further improved by omitting perfusion fixation and instead only fixing perfused and harvested organs by immersion in fixative, at the cost of a slightly lower quality of tissue fixation due to the 20–30 min polymerisation time of the casting agent. Furthermore, some artefacts relate to the preparation of the μAngiofil casting agent. The mixture was prepared and applied according to the manufacturer's guidelines. However, some air bubbles were found in perfused vessels, and the mixture of contrast agent and polyurethane carrier was not perfectly homogeneous, showing some highly attenuating droplets of contrast agent (Figure S1). These artefacts may not represent a general shortcoming of the method but rather reflect the limited experience of the experimenters with the casting procedure. Crucially, any quantitative microCT or microDECT examination of the vasculature requires validation of perfusion quality in the organ or tissue of interest using a complementary technique such as histology. Both barium sulphate crystals[15,84,85] and the μAngiofil casting agent[12,21] can be clearly identified in paraffin sections, allowing quantitative analysis of perfusion performance. For example, based on a correlative microCT and histology approach, Schaad et al.[12] determined a μAngiofil perfusion efficiency of 98% for capillaries in mouse soleus muscle, which is comparable to the perfusion efficiency determined for light sheet microscopic analysis of brain capillaries based on gel perfusion.[86]

Minor improvements could also be made regarding imaging protocols and beam hardening correction settings. Although the quality of spectral separation was generally high and only a small amount of beam hardening artefacts was observed in reconstructed 40 and 80 kVp image volumes, beam hardening can cause spectral artefacts that negatively affect the precision of the basis material decomposition procedure. In the presented datasets, spectral artefacts were limited to the vicinity of highly attenuating structures such as bone and teeth and highly attenuating droplets of contrast agent. In these regions, beam hardening can cause artificial intensity values in extracted material fractions. False positive intensity values may appear in the mineralised tissue (HA) material fraction in very dense areas of the casting agent, such as droplets of μAngiofil contrast agent that were not adequately mixed with the polyurethane carrier (Figure S12A). In a similar way, false positive intensity values may appear at the edges of bone and teeth in the casting agent material fraction (Figure S12B). Although beam hardening is a general limitation when imaging with polychromatic x-ray sources, we are confident that fine-tuning of x-ray filters and beam hardening correction settings will allow a further reduction of spectral artefacts. This is especially relevant when small vessels are analysed directly in the vicinity of bone.

4.5 | X-ray microCT versus light-optical modalities for 3D microscopic imaging of vasculature

In addition to microCT, various light-optical techniques have been successfully used for in situ 3D imaging of microscopic vascular architecture in ex vivo specimens.[79,86–89] In this section, a brief technical comparison between microCT and light sheet fluorescence microscopy (LSFM), high-resolution episcopic microscopy (HREM) and micro-optical section tomography (MOST) will be made, whereas the advantages and limitations of the different techniques for 3D vascular imaging have been discussed in detail in previous papers.[22,90,91]

Sample preparation for microCT imaging can be more straightforward compared to light-optical techniques, as

it does not require optical clearing or tissue embedding. If only vasculature and mineralised tissue are the focus of interest, microCT imaging can be performed directly after tissue fixation. However, if soft tissue is also the focus of interest, B-PTA counterstaining requires an additional several days to weeks, which makes sample preparation equally lengthy compared to light-optical staining and clearing methods[92–94] or tissue embedding procedures.[79,87,95]

MicroDECT scans require at least several hours depending on the type of scanner used and the required image resolution. With the scanner model used in the present study and full detector resolution (no binning), the dual-energy scans shown in the present work were overnight scans with a duration of at least 10–16 h, whereas some dual-energy scans lasted up to 24 h. When two regions are scanned and stitched vertically, the scan time doubles, whereas the scan time could also be reduced by detector binning or using larger flat panel detectors. When comparing image acquisition times for the mouse brain, microDECT image acquisition time was between the acquisition times reported for HREM (~8 h[95]) and MOST (~7 days[87]), whereas data acquisition is generally shorter for LSFM.[96]

The image resolution of microCT is isotropic. The voxel sizes used for imaging whole organs such as the brain (Ref. [22], present study) or the kidney[11] are usually in the range of 2–7 μm, so that at least blood vessels with a size of 6 μm or more can be spatially resolved when imaging whole mouse organs, whereas higher resolutions and isotropic voxel sizes of 1 μm and below can be achieved when imaging smaller FOVs. However, imaging of large FOVs at high resolution is easier with light-optical approaches, where smaller voxel sizes and thus higher resolutions can be achieved for entire mouse organs such as the brain (LSFM: very variable up to sub-micron lateral resolution, e.g. 0.45 μm × 0.46 μm × 2.91 μm resolution[97]; MOST: 0.35 μm × 0.35 μm × 1 μm[87]). Despite their anisotropic nature, this makes light-optical approaches the tool of choice for brain-wide cell analyses in conjunction with capillary network analysis. Image resolution and voxel size inevitably affect data size. Small voxel sizes obtained with LSFM and MOST for the whole mouse brain result in data sizes of 1–2.5 TB,[87,90,96] whereas the size of the reconstructed microDECT raw data for the brain shown in this work (isotropic voxel size = 5.42 μm) was only 64 GB. If the isotropic voxel size in a microDECT volume of the entire mouse brain were reduced to approximately 2.5 μm using a 4k × 4k detector, the reconstructed data size would be 512 GB.

The ability to image mineralised tissue, vasculature and soft tissue simultaneously in one sample (Figures 7–10) is unique to microCT and offers several interesting possibilities. However, typical microCT imaging applications lack molecular specificity, limiting the information obtained to the morphology of the vessels and their structural tissue context. In comparison, light-optical modalities such as LSFM can utilise a range of molecular markers that enable, for example, the differentiation of blood vessels from lymphatic vessels or mature blood vessels from capillaries[98] or arteries from veins.[88] In addition, light sheet microscopy can be used to, for example, simultaneously image vasculature and neurones in the brain.[86]

To summarise, each of these techniques has its merits and its own areas of application, and the choice of the most appropriate imaging modality is ultimately always highly dependent on the specific research question.

4.6 | Data processing workload

The workflow presented here involves a considerable amount of data processing after image acquisition. The time required for tomogram reconstruction and image processing is highly dependent on the software and computer hardware used. In the present case, the total computational time per dual-energy dataset (2048 × 2048 × 2048 voxels, 16 bit, 2 scan energies) was about 12 h, with the reconstruction of tomograms from raw projection data being the most time-consuming step (~8 h), followed by image resampling using the Lanczos algorithm (~2 h) and basis material decomposition (~1 h). Although the computational time is relatively long, the actual computational workload for the experimenter is only 2–3 h per dual-energy dataset. The most time-consuming part is the calculation of the intensity standardisation reference values and the calculation and validation of the basis material decomposition values. However, this only needs to be done once for a given energy pair and FOV, as these values can be applied to subsequent scans. More importantly, if microDECT with a well-defined FOV and sample type is used as a routine application, the entire data processing part could be fully automated in the future based on MATLAB or Python code, reducing the data processing workload for decomposing dual energy scans into material fractions to approximately 15–30 min.

4.7 | Applicability of the presented workflows to other samples, including other vertebrate species

In principle, the presented sample preparation and microDECT imaging workflows should be applicable to any vertebrate tissue sample up to a certain sample size. Three important aspects must be considered. (1) Perfusion:

μAngiofil perfusion has been demonstrated not only in mice but also in the rat and minipig.[22] Depending on the organ and tissue under consideration, a suitable perfusion access must be found to achieve complete perfusion of the ROI. In the case of μAngiofil, the amount of casting agent required is a limitation to the overall specimen size, as the commercially available μAngiofil kit is comparatively expensive and supplied in small quantities (~13 mL). This limits the use of μAngiofil to specimens a few centimetres in size. In comparison, Micropaque barium sulphate is much cheaper and available in larger quantities and could therefore be used for larger samples. (2) Resolution and FOV: As a general limitation in microCT imaging, the FOV used for imaging defines the achievable spatial image resolution. Therefore, high spatial resolutions are achieved with small FOVs, whereas the resolution decreases with a larger FOV.[49] Thus, the level of detail required, as defined by the investigator, places an inherent limit on the achievable FOV and sample size. If only larger arteries and veins are of interest, comparatively large FOVs can be achieved. If smaller arterioles and venules (~10–100 μm diameter) are of interest, the FOV must be limited to 2 cm or less. If the capillary bed is the focus of analysis, the FOV will typically be only a few millimetres. (3) B-PTA counterstain: PTA staining has been demonstrated to be effective on a diverse array of animal tissues.[48,99] Despite the relatively slow rate of tissue penetration, which is attributed to the large molecular weight of PTA, this method has been shown to produce homogeneous staining in samples larger than 1 cm (Figure 7). Staining samples up to several centimetres in size seems feasible. However, it is essential to test and validate this approach for each sample type, as the staining process is strongly dependent on the tissue type and fixative used. In general, the workflows described are applicable to most vertebrate samples, ranging in size from a few millimetres to a few centimetres. In the event that only large arteries are of interest and B-PTA counterstaining is not required, imaging of barium sulphate–perfused vessels in the context of mineralised skeleton can be performed also on larger specimens up to ~20 cm in size.

5 | OUTLOOK

In the present paper, we introduced an ex vivo spectral microscopic dual energy imaging approach that allows to generate high contrast datasets of vascular architecture together with data on general skeletal and soft tissue morphology in samples such as the mouse head and brain. By combining vasculature and reference tissue information in a single-imaging modality and a single-sample preparation step, the presented approach expands the toolbox for vascular phenotyping in laboratory animal models, as demonstrated for visualisation and segmentation of vascularisation of the murine mandible in a recent preprint.[100] Recently, huge advancements have been made concerning the automated segmentation and analysis of vasculature.[88,89,101–104] In combination with 3D atlases that allow accurate vasculature localisation,[87] it seems feasible that analysis of vascular phenotypes with reference to general tissue morphology can be conducted in a fully automated fashion for a variety of different organ systems.

ACKNOWLEDGEMENTS

We thank Thomas Kolbe of the Centre of Biological Sciences of Vetmeduni Vienna (unit 'In vivo and in vitro models') for providing mice. This research was supported using resources of the VetCore Facility (VetImaging) of the University of Veterinary Medicine Vienna.

CONFLICT OF INTEREST STATEMENT

The authors declare no conflicts of interest.

DATA AVAILABILITY STATEMENT

All data presented in this study are available from the corresponding author (SH) upon reasonable request.

REFERENCES

1. Skutta, B., Furst, G., Eilers, J., Ferbert, A., & Kuhn, F. P. (1999). Intracranial stenoocclusive disease: Double-detector helical CT angiography versus digital subtraction angiography. *American Journal of Neuroradiology*, *20*(5), 791–799.
2. Fleischmann, D., Hallett, R. L., & Rubin, G. D. (2006). CT angiography of peripheral arterial disease. *Journal of Vascular and Interventional Radiology*, *17*(1), 3–26.
3. Plank, F., Friedrich, G., Dichtl, W., Klauser, A., Jaschke, W., Franz, W.-M., & Feuchtner, G. (2014). The diagnostic and prognostic value of coronary CT angiography in asymptomatic high-risk patients: A cohort study. *Open Heart*, *1*(1), e000096.
4. Bae, K. T. (2010). Intravenous contrast medium administration and scan timing at CT: Considerations and approaches. *Radiology*, *256*(1), 32–61.
5. Lusic, H., & Grinstaff, M. W. (2013). X-ray-computed tomography contrast agents. *Chemical Reviews*, *113*(3), 1641–1666.
6. Holdsworth, D. W., & Thornton, M. M. (2002). Micro-CT in small animal and specimen imaging. *Trends in Biotechnology*, *20*(8), S34–S39.
7. Starosolski, Z., Villamizar, C. A., Rendon, D., Paldino, M. J., Milewicz, D. M., Ghaghada, K. B., & Annapragada, A. V. (2015). Ultra high-resolution in vivo computed tomography imaging of mouse cerebrovasculature using a long circulating blood pool contrast agent. *Scientific Reports*, *5*, 10178.
8. Sawall, S., Beckendorf, J., Amato, C., Maier, J., Backs, J., Vande Velde, G., Kachelrieß, M., & Kuntz, J. (2020). Coronary micro-computed tomography angiography in mice. *Scientific Reports*, *10*(1), 16866.
9. Grabherr, S., Djonov, V., Yen, K., Thali, M. J., & Dirnhofer, R. (2007). Postmortem angiography: Review of former and current methods. *American Journal of Roentgenology*, *188*(3), 832–838.

10. Leyssens, L., Pestiaux, C., & Kerckhofs, G. (2021). A review of ex vivo X-ray microfocus computed tomography-based characterization of the cardiovascular system. *International Journal of Molecular Sciences*, *22*(6), 3263.
11. Hlushchuk, R., Zubler, C., Barré, S., Correa Shokiche, C., Schaad, L., Röthlisberger, R., Wnuk, M., Daniel, C., Khoma, O., Tschanz, S. A., Reyes, M., & Djonov, V. (2018). Cutting-edge microangio-CT: New dimensions in vascular imaging and kidney morphometry. *American Journal of Physiology. Renal Physiology*, *314*(3), F493–F499.
12. Schaad, L., Hlushchuk, R., Barré, S., Gianni-Barrera, R., Haberthür, D., Banfi, A., & Djonov, V. (2017). Correlative imaging of the murine hind limb vasculature and muscle tissue by MicroCT and light microscopy. *Scientific Reports*, *7*, 41842.
13. Heimel, P., Swiadek, N. V., Slezak, P., Kerbl, M., Schneider, C., Nürnberger, S., Redl, H., Teuschl, A. H., & Hercher, D. (2019). Iodine-enhanced micro-CT imaging of soft tissue on the example of peripheral nerve regeneration. *Contrast Media and Molecular Imaging*, *2019*, 7483745.
14. Margolis, R., Merlo, B., Chanthavisay, D., Chavez, C., Trinh, B., & Li, J. (2024). Comparison of micro-CT image enhancement after use of different vascular casting agents. *Quantitative Imaging in Medicine and Surgery*, *14*(3), 2568–2579.
15. Sider, K. L., Song, J., & Davies, J. E. (2010). A new bone vascular perfusion compound for the simultaneous analysis of bone and vasculature. *Microscopy Research and Technique*, *73*(7), 665–672.
16. Hong, S.-H., Herman, A. M., Stephenson, J. M., Wu, T., Bahadur, A. N., Burns, A. R., Marrelli, S. P., & Wythe, J. D. (2020). Development of barium-based low viscosity contrast agents for micro CT vascular casting: Application to 3D visualization of the adult mouse cerebrovasculature. *Journal of Neuroscience Research*, *98*(2), 312–324.
17. Roche, B., Vanden-Bossche, A., Malaval, L., Normand, M., Jannot, M., Chaux, R., Vico, L., & Lafage-Proust, M.-H. (2014). Parathyroid hormone 1–84 targets bone vascular structure and perfusion in mice: Impacts of its administration regimen and of ovariectomy. *Journal of Bone and Mineral Research: The Official Journal of the American Society for Bone and Mineral Research*, *29*(7), 1608–1618.
18. Fei, J., Peyrin, F., Malaval, L., Vico, L., & Lafage-Proust, M. H. (2010). Imaging and quantitative assessment of long bone vascularization in the adult rat using microcomputed tomography. *Anatomical Record (Hoboken)*, *293*(2), 215–224.
19. Grabherr, S., Dominietto, M., Yu, L., Djonov, V., Müller, B., & Friess, S. (2008). Angiofil: A novel radio-contrast agent for post-mortem microangiography. In S. R. Stock (Ed.), *Developments in X-ray tomography VI* (vol. 7078, pp. 70781O-1–70781O-8). Proceedings of the SPIE.
20. Grabherr, S., Hess, A., Karolczak, M., Thali, M. J., Friess, S. D., Kalender, W. A., Dirnhofer, R., & Djonov, V. (2008). Angiofil-mediated visualization of the vascular system by microcomputed tomography: A feasibility study. *Microscopy Research and Technique*, *71*(7), 551–556.
21. Hlushchuk, R., Haberthür, D., & Djonov, V. (2019). Ex vivo microangioCT: Advances in microvascular imaging. *Vascular Pharmacology*, *112*, 2–7.
22. Hlushchuk, R., Haberthür, D., Soukup, P., Barré, S. F., Khoma, O.-Z., Schittny, J., Haghayegh Jahromi, N., Bouchet, A., Engelhardt, B., & Djonov, V. (2020). Innovative high-resolution microCT imaging of animal brain vasculature. *Brain Structure and Function*, *225*(9), 2885–2895.
23. Kingston, M. J., Perriman, D. M., Neeman, T., Smith, P. N., & Webb, A. L. (2016). Contrast agent comparison for three-dimensional micro-CT angiography: A cadaveric study. *Contrast Media and Molecular Imaging*, *11*(4), 319–324.
24. Granton, P. V., Pollmann, S. I., Ford, N. L., Drangova, M., & Holdsworth, D. W. (2008). Implementation of dual- and triple-energy cone-beam micro-CT for postreconstruction material decomposition. *Medical Physics*, *35*(11), 5030–5042.
25. Ghanavati, S., Yu, L. X., Lerch, J. P., & Sled, J. G. (2014). A perfusion procedure for imaging of the mouse cerebral vasculature by X-ray micro-CT. *Journal of Neuroscience Methods*, *221*, 70–77.
26. Weyers, J. J., Carlson, D. D., Murry, C. E., Schwartz, S. M., & Mahoney, W. M., Jr. (2012). Retrograde perfusion and filling of mouse coronary vasculature as preparation for micro computed tomography imaging. *Journal of Visualized Experiments*, (60), e3740.
27. Redenski, I., Guo, S., Machour, M., Szklanny, A., Landau, S., Egozi, D., Gabet, Y., & Levenberg, S. (2022). Microcomputed tomography-based analysis of neovascularization within bio-engineered vascularized tissues. *ACS Biomaterials Science & Engineering*, *8*(1), 232–241.
28. Lametschwandtner, A., & Minnich, B. (2021). Scanning electron microscopy of vascular corrosion casts in biological and biomedical research. *Journal of Morphology and Anatomy*, *5*(1), 1–5.
29. Quintana, D. D., Lewis, S. E., Anantula, Y., Garcia, J. A., Sarkar, S. N., Cavendish, J. Z., Brown, C. M., & Simpkins, J. W. (2019). The cerebral angiome: High resolution MicroCT imaging of the whole brain cerebrovasculature in female and male mice. *Neuroimage*, *202*, 116109.
30. Stock, S. R. (2020). *MicroComputed tomography: Methodology and applications* (2nd ed.). CRC Press/Taylor & Francis Group.
31. Boone, M. N., Garrevoet, J., Tack, P., Scharf, O., Cormode, D. P., van Loo, D., Pauwels, E., Dierick, M., Vincze, L., & Van Hoorebeke, L. (2014). High spectral and spatial resolution X-ray transmission radiography and tomography using a Color X-ray Camera. *Nuclear Instruments & Methods in Physics Research. Section A, Accelerators, Spectrometers, Detectors and Associated Equipment*, *735*, 644–648.
32. Johnson, T. R. (2012). Dual-energy CT: General principles. *American Journal of Roentgenology*, *199*(5 Suppl), S3–S8.
33. Maier, D. S., Schock, J., & Pfeiffer, F. (2017). Dual-energy micro-CT with a dual-layer, dual-color, single-crystal scintillator. *Optics Express*, *25*(6), 6924–6935.
34. Egan, C. K., Jacques, S. D. M., Wilson, M. D., Veale, M. C., Seller, P., Beale, A. M., Pattrick, R. A. D., Withers, P. J., & Cernik, R. J. (2015). 3D chemical imaging in the laboratory by hyperspectral X-ray computed tomography. *Scientific Reports*, *5*, 15979.
35. Warr, R., Handschuh, S., Glösmann, M., Cernik, R. J., & Withers, P. J. (2022). Quantifying multiple stain distributions in bioimaging by hyperspectral X-ray tomography. *Scientific Reports*, *12*(1), 21945.
36. Achenbach, S., Moselewski, F., Ropers, D., Ferencik, M., Hoffmann, U., Macneill, B., Pohle, K., Baum, U., Anders,

K., Jang, I.-K., Daniel, W. G., & Brady, T. J. (2004). Detection of calcified and noncalcified coronary atherosclerotic plaque by contrast-enhanced, submillimeter multidetector spiral computed tomography: A segment-based comparison with intravascular ultrasound. *Circulation*, *109*(1), 14–17.

37. Acharya, S., Goyal, A., Bhalla, A. S., Sharma, R., Seth, A., & Gupta, A. K. (2015). In vivo characterization of urinary calculi on dual-energy CT: Going a step ahead with sub-differentiation of calcium stones. *Acta Radiologica*, *56*(7), 881–889.
38. Zhang, L.-J., Wu, S.-Y., Niu, J.-B., Zhang, Z.-L., Wang, H. Z., Zhao, Y.-E., Chai, X., Zhou, C.-S., & Lu, G.-M. (2010). Dual-energy CT angiography in the evaluation of intracranial aneurysms: Image quality, radiation dose, and comparison with 3D rotational digital subtraction angiography. *American Journal of Roentgenology*, *194*(1), 23–30.
39. Badea, C. T., Guo, X., Clark, D., Johnston, S. M., Marshall, C. D., & Piantadosi, C. A. (2012). Dual-energy micro-CT of the rodent lung. *American Journal of Physiology. Lung Cellular and Molecular Physiology*, *302*(10), L1088–L1097.
40. Badea, C. T., Befera, N., Clark, D., Qi, Y., & Johnson, G. A. (2014). Dual-energy micro-CT imaging of pulmonary airway obstruction: Correlation with micro-SPECT. *Proceedings of the SPIE*, *9038*, 90380U.
41. Ashton, J. R., Clark, D. P., Moding, E. J., Ghaghada, K., Kirsch, D. G., West, J. L., & Badea, C. T. (2014). Dual-energy micro-CT functional imaging of primary lung cancer in mice using gold and iodine nanoparticle contrast agents: A validation study. *PLoS ONE*, *9*(2), e88129.
42. Handschuh, S., Beisser, C. J., Ruthensteiner, B., & Metscher, B. D. (2017). Microscopic dual-energy CT (microDECT): A flexible tool for multichannel ex vivo 3D imaging of biological specimens. *Journal of Microscopy*, *267*(1), 3–26.
43. Schulz, B., Kuehling, K., Kromen, W., Siebenhandl, P., Kerl, M. J., Vogl, T. J., & Bauer, R. (2012). Automatic bone removal technique in whole-body dual-energy CT angiography: Performance and image quality. *American Journal of Roentgenology*, *199*(5), W646–W650.
44. Watanabe, Y., Uotani, K., Nakazawa, T., Higashi, M., Yamada, N., Hori, Y., Kanzaki, S., Fukuda, T., Itoh, T., & Naito, H. (2009). Dual-energy direct bone removal CT angiography for evaluation of intracranial aneurysm or stenosis: Comparison with conventional digital subtraction angiography. *European Radiology*, *19*(4), 1019–1024.
45. Zboray, R., Schweitzer, W., Ebert, L., Wolf, M., Guglielmini, S., Haemmerle, S., Weiss, S., & Koller, B. (2024). Development of a micro-CT scanner with dual-energy option and endovascular contrast agent administration protocol for fetal and neonatal virtual autopsy. *Journal of Imaging*, *10*(3), 60.
46. Zysk, A. M., Garson, A. B., Xu, Q., Brey, E. M., Zhou, W., Brankov, J. G., Wernick, M. N., Kuszak, J. R., & Anastasio, M. A. (2012). Nondestructive volumetric imaging of tissue microstructure with benchtop x-ray phase-contrast tomography and critical point drying. *Biomedical Optics Express*, *3*(8), 1924–1932.
47. Patzelt, M., Mrzilkova, J., Dudak, J., Krejci, F., Zemlicka, J., Karch, J., Musil, V., Rosina, J., Sykora, V., Horehledova, B., & Zach, P. (2019). Ethanol fixation method for heart and lung imaging in micro-CT. *Japanese Journal of Radiology*, *37*(6), 500–510.
48. Metscher, B. D. (2009). MicroCT for comparative morphology: Simple staining methods allow high-contrast 3D imaging of diverse non-mineralized animal tissues. *BMC Physiology*, *9*, 11.
49. Handschuh, S., & Glösmann, M. (2022). Mouse embryo phenotyping using X-ray microCT. *Frontiers in Cell and Developmental Biology*, *10*, 949184.
50. Busse, M., Müller, M., Kimm, M. A., Ferstl, S., Allner, S., Achterhold, K., Herzen, J., & Pfeiffer, F. (2018). Three-dimensional virtual histology enabled through cytoplasm-specific X-ray stain for microscopic and nanoscopic computed tomography. *Proceedings of the National Academy of Sciences of the United States of America*, *115*(10), 2293–2298.
51. Cockman, M. D., Blanton, C. A., Chmielewski, P. A., Dong, L., Dufresne, T. E., Hookfin, E. B., Karb, M. J., Liu, S., & Wehmeyer, K. R. (2006). Quantitative imaging of proteoglycan in cartilage using a gadolinium probe and microCT. *Osteoarthritis and Cartilage*, *14*(3), 210–214.
52. Martins De Souza e Silva, J., Utsch, J., Kimm, M. A., Allner, S., Epple, M. F., Achterhold, K., & Pfeiffer, F. (2017). Dual-energy micro-CT for quantifying the time-course and staining characteristics of ex-vivo animal organs treated with iodine- and gadolinium-based contrast agents. *Scientific Reports*, *7*(1), 17387.
53. Mizutani, R., & Suzuki, Y. (2012). X-ray microtomography in biology. *Micron (Oxford, England: 1993)*, *43*(2–3), 104–115.
54. Metscher, B. D. (2009). MicroCT for developmental biology: A versatile tool for high-contrast 3D imaging at histological resolutions. *Developmental Dynamics: An Official Publication of the American Association of Anatomists*, *238*(3), 632–640.
55. Müller, M., Kimm, M. A., Ferstl, S., Allner, S., Achterhold, K., Herzen, J., Pfeiffer, F., & Busse, M. (2018). Nucleus-specific X-ray stain for 3D virtual histology. *Scientific Reports*, *8*(1), 17855.
56. Metscher, B. (2021). A simple nuclear contrast staining method for microCT-based 3D histology using lead(II) acetate. *Journal of Anatomy*, *238*(4), 1036–1041.
57. Golding, R. E., & Jones, A. S. (2007). Micro-CT as a novel technique for 3D reconstruction of molluscan anatomy. *Molluscan Research*, *27*(3), 123–128.
58. Descamps, E., Sochacka, A., de Kegel, B., van Loo, D., van Hoorebeke, L., & Adriaens, D. (2014). Soft tissue discrimination with contrast agents using micro-CT scanning. *Belgian Journal of Zoology*, *144*(1), 20–40.
59. Johnson, J. T., Hansen, M. S., Wu, I., Healy, L. J., Johnson, C. R., Jones, G. M., Capecchi, M. R., & Keller, C. (2006). Virtual histology of transgenic mouse embryos for high-throughput phenotyping. *PLoS Genetics*, *2*(4), e61.
60. Gabner, S., Böck, P., Fink, D., Glösmann, M., & Handschuh, S. (2020). The visible skeleton 2.0: Phenotyping of cartilage and bone in fixed vertebrate embryos and foetuses based on X-ray microCT. *Development (Cambridge, England)*, *147*(11), dev187633.
61. Gignac, P. M., Kley, N. J., Clarke, J. A., Colbert, M. W., Morhardt, A. C., Cerio, D., Cost, I. N., Cox, P. G., Daza, J. D., Early, C. M., Echols, M. S., Henkelman, R. M., Herdina, A. N., Holliday, C. M., Li, Z., Mahlow, K., Merchant, S., Müller, J., Orsbon, C. P., … Witmer, L. M. (2016). Diffusible iodine-based contrast-enhanced computed tomography (diceCT): An emerging tool for rapid, high-resolution, 3-D imaging of metazoan soft tissues. *Journal of Anatomy*, *228*(6), 889–909.

62. Sombke, A., Lipke, E., Michalik, P., Uhl, G., & Harzsch, S. (2015). Potential and limitations of X-ray micro-computed tomography in arthropod neuroanatomy: A methodological and comparative survey. *Journal of Comparative Neurology*, *523*(8), 1281–1295.
63. Close, B., Banister, K., Baumans, V., Bernoth, E.-M., Bromage, N., Bunyan, J., Erhardt, W., Flecknell, P., Gregory, N., Hackbarth, H., Morton, D., & Warwick, C. (1997). Recommendations for euthanasia of experimental animals: Part 2. DGXT of the European Commission. *Laboratory Animals*, *31*(1), 1–32.
64. Leary, S. L. (2020). *AVMA guidelines for the euthanasia of animals*. American Veterinary Medical Association.
65. Hubbel, J. H., & Seltzer, S. M. (2004). *Tables of X-ray mass attenuation coefficients and mass energy-absorption coefficients* (version 1.4). National Institute of Standards and Technology. http://physics.nist.gov/xaamdi
66. Boone, J. M., Fewell, T. R., & Jennings, R. J. (1997). Molybdenum, rhodium, and tungsten anode spectral models using interpolating polynomials with application to mammography. *Medical Physics*, *24*(12), 1863–1874.
67. Boone, J. M., & Seibert, J. A. (1997). An accurate method for computer-generating tungsten anode x-ray spectra from 30 to 140 kV. *Medical Physics*, *24*(11), 1661–1670.
68. Fewell, T. R., Shuping, R., & Healy, K. (1981). *Handbook of computed tomography X-ray spectra*. U.S. Government Printing Office.
69. Dawood, Y., Hagoort, J., Siadari, B. A., Ruijter, J. M., Gunst, Q. D., Lobe, N. H. J., Strijkers, G. J., De Bakker, B. S., & Van Den Hoff, M. J. B. (2021). Reducing soft-tissue shrinkage artefacts caused by staining with Lugol's solution. *Scientific Reports*, *11*(1), 19781.
70. Schindelin, J., Arganda-Carreras, I., Frise, E., Kaynig, V., Longair, M., Pietzsch, T., Preibisch, S., Rueden, C., Saalfeld, S., Schmid, B., Tinevez, J.-Y., White, D. J., Hartenstein, V., Eliceiri, K., Tomancak, P., & Cardona, A. (2012). Fiji: An open-source platform for biological-image analysis. *Nature Methods*, *9*(7), 676–682.
71. Limaye, A. (2012). Drishti, a volume exploration and presentation tool. *Proceedings of the SPIE*, *8506*, 85060X.
72. Haberthür, D., Khoma, O.-Z., Hoessly, T., Zoni, E., Kruithof-de Julio, M., Ryan, S. D., Grunewald, M., Bellón, B., Sandgren, R., Handschuh, S., Pippenger, B. E., Bosshardt, D., Djonov, V., & Hlushchuk, R. (2023). MicroCT-based imaging of microvasculature within the bone tissue. *bioRxiv*. https://doi.org/10.1101/2023.03.08.531678. Version 2: 2023, 1-18.
73. Rosenblum, J. S., Cappadona, A. J., Lookian, P. P., Chandrashekhar, V., Bryant, J.-P., Chandrashekhar, V., Zhao, D. Y., Knutsen, R. H., Donahue, D. R., Mcgavern, D. B., Kozel, B. A., Heiss, J. D., Pacak, K., & Zhuang, Z. (2022). Non-invasive in situ visualization of the murine cranial vasculature. *Cell Reports Methods*, *2*(1), 100151.
74. Bhargava, A., Monteagudo, B., Kushwaha, P., Senarathna, J., Ren, Y., Riddle, R. C., Aggarwal, M., & Pathak, A. P. (2022). VascuViz: A multimodality and multiscale imaging and visualization pipeline for vascular systems biology. *Nature Methods*, *19*(2), 242–254.
75. Wang, Q., Ding, S.-L., Li, Y., Royall, J., Feng, D., Lesnar, P., Graddis, N., Naeemi, M., Facer, B., Ho, A., Dolbeare, T., Blanchard, B., Dee, N., Wakeman, W., Hirokawa, K. E., Szafer, A., Sunkin, S. M., Oh, S. W., Bernard, A., … Ng, L. (2020). The Allen mouse brain common coordinate framework: A 3D reference atlas. *Cell*, *181*(4), 936–953.e20.
76. Blery, P., Pilet, P., Vanden-Bossche, A., Thery, A., Guicheux, J., Amouriq, Y., Espitalier, F., Mathieu, N., & Weiss, P. (2016). Vascular imaging with contrast agent in hard and soft tissues using microcomputed-tomography. *Journal of Microscopy*, *262*(1), 40–49.
77. Caradu, C., Guy, A., James, C., Reynaud, A., Gadeau, A.-P., & Renault, M.-A. (2018). Endogenous Sonic Hedgehog limits inflammation and angiogenesis in the ischaemic skeletal muscle of mice. *Cardiovascular Research*, *114*(5), 759–770.
78. Oses, P., Renault, M.-A., Chauvel, R., Leroux, L., Allières, C., Séguy, B., Lamazière, J.-M. D., Dufourcq, P., Couffinhal, T., & Duplàa, C. (2009). Mapping 3-dimensional neovessel organization steps using micro-computed tomography in a murine model of hindlimb ischemia-brief report. *Arteriosclerosis, Thrombosis, and Vascular Biology*, *29*(12), 2090–2092.
79. Zopf, L. M., Heimel, P., Geyer, S. H., Kavirayani, A., Reier, S., Fröhlich, V., Stiglbauer-Tscholakoff, A., Chen, Z., Nics, L., Zinnanti, J., Drexler, W., Mitterhauser, M., Helbich, T., Weninger, W. J., Slezak, P., Obenauf, A., Bühler, K., & Walter, A. (2021). Cross-modality imaging of murine tumor vasculature-a feasibility study. *Molecular Imaging and Biology: MIB: The Official Publication of the Academy of Molecular Imaging*, *23*(6), 874–893.
80. Plouraboué, F., Cloetens, P., Fonta, C., Steyer, A., Lauwers, F., & Marc-Vergnes, J.-P. (2004). X-ray high-resolution vascular network imaging. *Journal of Microscopy-Oxford*, *215*(Pt. 2), 139–148.
81. Buytaert, J., Goyens, J., de Greef, D., Aerts, P., & Dirckx, J. (2014). Volume shrinkage of bone, brain and muscle tissue in sample preparation for micro-CT and light sheet fluorescence microscopy (LSFM). *Microscopy and Microanalysis*, *20*(4), 1208–1217.
82. Kerckhofs, G., Stegen, S., Van Gastel, N., Sap, A., Falgayrac, G., Penel, G., Durand, M., Luyten, F. P., Geris, L., Vandamme, K., Parac-Vogt, T., & Carmeliet, G. (2018). Simultaneous three-dimensional visualization of mineralized and soft skeletal tissues by a novel microCT contrast agent with polyoxometalate structure. *Biomaterials*, *159*, 1–12.
83. de Bournonville, S., Vangrunderbeeck, S., Ly, H. G. T., Geeroms, C., de Borggraeve, W. M., Parac-Vogt, T. N., & Kerckhofs, G. (2020). Exploring polyoxometalates as non-destructive staining agents for contrast-enhanced microfocus computed tomography of biological tissues. *Acta Biomaterialia*, *105*, 253–262.
84. Hultborn, R., Weiss, L., Tveit, E., Lange, S., Jennische, E., Erlandsson, M. C., & Johansson, M. E. (2024). Ex vivo vascular imaging and perfusion studies of normal kidney and tumor vasculature. *Cancers*, *16*(10), 1939.
85. Haakma, W., Rohde, M., Kuster, L., Uhrenholt, L., Pedersen, M., & Boel, L. W. T. (2016). Post-mortem computed tomography angiography utilizing barium sulfate to identify microvascular structures: A preliminary phantom model and case study. *Journal of Forensic Radiology and Imaging*, *7*, 38–42.
86. Di Giovanna, A. P., Tibo, A., Silvestri, L., Müllenbroich, M. C., Costantini, I., Allegra Mascaro, A. L., Sacconi, L., Frasconi, P., & Pavone, F. S. (2018). Whole-brain vasculature

reconstruction at the single capillary level. *Scientific Reports*, *8*(1), 12573.
87. Xiong, B., Li, A., Lou, Y., Chen, S., Long, B., Peng, J., Yang, Z., Xu, T., Yang, X., Li, X., Jiang, T., Luo, Q., & Gong, H. (2017). Precise cerebral vascular atlas in stereotaxic coordinates of whole mouse brain. *Frontiers in Neuroanatomy*, *11*, 128.
88. Kirst, C., Skriabine, S., Vieites-Prado, A., Topilko, T., Bertin, P., Gerschenfeld, G., Verny, F., Topilko, P., Michalski, N., Tessier-Lavigne, M., & Renier, N. (2020). Mapping the fine-scale organization and plasticity of the brain vasculature. *Cell*, *180*(4), 780–795.e25.
89. Todorov, M. I., Paetzold, J. C., Schoppe, O., Tetteh, G., Shit, S., Efremov, V., Todorov-Völgyi, K., Düring, M., Dichgans, M., Piraud, M., Menze, B., & Ertürk, A. (2020). Machine learning analysis of whole mouse brain vasculature. *Nature Methods*, *17*(4), 442–449.
90. Bennett, H. C., & Kim, Y. (2022). Advances in studying whole mouse brain vasculature using high-resolution 3D light microscopy imaging. *Neurophotonics*, *9*(2), 21902.
91. Epah, J., Pálfi, K., Dienst, F. L., Malacarne, P. F., Bremer, R., Salamon, M., Kumar, S., Jo, H., Schürmann, C., & Brandes, R. P. (2018). 3D imaging and quantitative analysis of vascular networks: A comparison of ultramicroscopy and micro-computed tomography. *Theranostics*, *8*(8), 2117–2133.
92. Costantini, I., Ghobril, J.-P., Di Giovanna, A. P., Mascaro, A. L. A., Silvestri, L., Müllenbroich, M. C., Onofri, L., Conti, V., Vanzi, F., Sacconi, L., Guerrini, R., Markram, H., Iannello, G., & Pavone, F. S. (2015). A versatile clearing agent for multi-modal brain imaging. *Scientific Reports*, *5*, 9808.
93. Liu, A. K. L., Hurry, M. E. D., Ng, O. T. W., Defelice, J., Lai, H. M., Pearce, R. K. B., Wong, G. T.-C., Chang, R. C.-C., & Gentleman, S. M. (2016). Bringing CLARITY to the human brain: Visualization of Lewy pathology in three dimensions. *Neuropathology and Applied Neurobiology*, *42*(6), 573–587.
94. Zhang, D., Cleveland, A. H., Krimitza, E., Han, K., Yi, C., Stout, A. L., Zou, W., Dorsey, J. F., Gong, Y., & Fan, Y. (2024). Spatial analysis of tissue immunity and vascularity by light sheet fluorescence microscopy. *Nature Protocols*, *19*(4), 1053–1082.
95. Mitchell, B., Mu, E., Currey, L., Whitehead, D., Walters, S., Thor, S., Kasherman, M., & Piper, M. (2024). A protocol for high-resolution episcopic microscopy and 3D volumetric analyses of the adult mouse brain. *Neuroscience Letters*, *824*, 137675.
96. Jiang, T., Gong, H., & Yuan, J. (2023). Whole-brain optical imaging: A powerful tool for precise brain mapping at the mesoscopic level. *Neuroscience Bulletin*, *39*(12), 1840–1858.
97. Glaser, A. K., Bishop, K. W., Barner, L. A., Susaki, E. A., Kubota, S. I., Gao, G., Serafin, R. B., Balaram, P., Turschak, E., Nicovich, P. R., Lai, H., Lucas, L. A. G., Yi, Y., Nichols, E. K., Huang, H., Reder, N. P., Wilson, J. J., Sivakumar, R., Shamskhou, E., … Liu, J. T. C. (2022). A hybrid open-top light-sheet microscope for versatile multi-scale imaging of cleared tissues. *Nature Methods*, *19*(5), 613–619.
98. Takahashi, K., Abe, K., Kubota, S. I., Fukatsu, N., Morishita, Y., Yoshimatsu, Y., Hirakawa, S., Kubota, Y., Watabe, T., Ehata, S., Ueda, H. R., Shimamura, T., & Miyazono, K. (2022). An analysis modality for vascular structures combining tissue-clearing technology and topological data analysis. *Nature Communications*, *13*(1), 5239.
99. Lesciotto, K. M., Motch Perrine, S. M., Kawasaki, M., Stecko, T., Ryan, T. M., Kawasaki, K., & Richtsmeier, J. T. (2020). Phosphotungstic acid-enhanced microCT: Optimized protocols for embryonic and early postnatal mice. *Developmental Dynamics*, *249*(4), 573–585.
100. Haberthür, D., Khoma, O.-Z., Hoessly, T., Zoni, E., Julio, M. K., Ryan, S. D., Grunewald, M., Bellón, B., Sandgren, R., Handschuh, S., Pippenger, B. E., Bosshardt, D., Djonov, V., & Hlushchuk, R. (2024). MicroCT-based imaging of microvasculature within bone and peri-implant tissues. *bioRxiv*. https://doi.org/10.1101/2023.03.08.531678. Version 3: 2024, 1-25.
101. Spangenberg, P., Hagemann, N., Squire, A., Förster, N., Krauß, S. D., Qi, Y., Mohamud Yusuf, A., Wang, J., Grüneboom, A., Kowitz, L., Korste, S., Totzeck, M., Cibir, Z., Tuz, A. A., Singh, V., Siemes, D., Struensee, L., Engel, D. R., Ludewig, P., … Mosig, A. (2023). Rapid and fully automated blood vasculature analysis in 3D light-sheet image volumes of different organs. *Cell Reports Methods*, *3*(3), 100436.
102. Li, Y., Liu, X., Jia, X., Jiang, T., Wu, J., Zhang, Q., Li, J., Li, X., & Li, A. (2023). A high-performance deep-learning-based pipeline for whole-brain vasculature segmentation at the capillary resolution. *Bioinformatics*, *39*(4), btad145.
103. Chadwick, E. A., Suzuki, T., George, M. G., Romero, D. A., Amon, C., Waddell, T. K., Karoubi, G., & Bazylak, A. (2021). Vessel network extraction and analysis of mouse pulmonary vasculature via X-ray micro-computed tomographic imaging. *PLoS Computational Biology*, *17*(4), e1008930.
104. Xu, H., & Langer, M. (2023). Quantitative analysis of bone, blood vessels, and metastases in mice tibiae using synchrotron radiation micro-computed tomography. *Cancers*, *15*(23), 5609.

SUPPORTING INFORMATION

Additional supporting information can be found online in the Supporting Information section at the end of this article.

How to cite this article: Handschuh, S., Reichart, U., Kummer, S., & Glösmann, M. (2025). In situ isotropic 3D imaging of vasculature perfusion specimens using x-ray microscopic dual-energy CT. *Journal of Microscopy*, *297*, 179–202. https://doi.org/10.1111/jmi.13369